HOKKAIDO UNIVERSITY

Title	Linear and nonlinear stability analyses of shallow open-channel flow with lateral velocity gradients
Author(s)	de Lima, Adriano Coutinho
Citation	北海道大学. 博士(工学) 甲第11054号
Issue Date	2013-06-28
DOI	10.14943/doctoral.k11054
Doc URL	http://hdl.handle.net/2115/53228
Type	theses (doctoral)
File Information	Adriano_Lima.pdf

Instructions for use

Hokkaido University Collection of Scholarly and Academic Papers : HUSCAP

Linear and nonlinear stability analyses of shallow open-channel flow with lateral velocity gradients

by

Adriano Coutinho de Lima

A dissertation submitted in partial fulfillment of the requirements for the degree of Doctor of Engineering

Examination Committee: Prof. Norihiro Izumi
Prof. Toshihiko Yamashita
Assoc. Prof. Tomohito Yamada

Division of Field Engineering for Environment
Graduate School of Engineering, Hokkaido University
June 2013

Abstract

The presence of vegetation is commonly observed in both natural and rectified watercourses. Vegetation in watercourses is desirable in some cases as it prevents bank erosion and provides habitat and food for numerous species. On the other hand, vegetation causes serious problems in other cases as it increases channel resistance and reduces channel capacity for the draining of flood water. Vegetation in a part of a channel produces transverse shear flow, which may lead to flow instability and the generation of large-scale horizontal vortices. These horizontal vortices have a strong influence on the velocity distribution and the amount of discharge conveyed by a channel without overflow, and enhance the lateral mixing of not only the flow itself, but also the substances transported by the flow both inside and outside the vegetated area. Therefore, it is important to determine the conditions under which instability occurs, and the characteristics of the horizontal vortices from both an engineering and an environmental points of view.

In this study we performed linear and nonlinear stability analyses of the flow in an open-channel partially covered with vegetation. We assume that the base state flow field before the occurrence of instability is characterized by turbulence, with a smaller length scale than the flow depth, which is mainly generated by the bottom friction. By introducing perturbations to the flow depth as well as the streamwise and transverse velocities in the base state, the conditions required for perturbations grow in time were studied over a wide range of (1) Froude number, (2) normalized non-vegetated zone width, and three other dimensionless parameters which represent the relative effect of (3) bed friction, (4) vegetation drag and (5) sub-depth eddy viscosity. The characteristic vortex shedding frequencies associated with the maximum growth rate was compared with those observed in experiments. Although the linear analysis was shown to be capable of predicting the order of magnitude of the frequencies, there is a systematic discrepancy between the predicted and observed frequencies which may be due to the limitation of linear stability analysis.

The nonlinear development of the perturbations was studied by means of a weakly nonlinear stability analysis. Our results indicated that supercritical bifurcation, where the amplitude of the perturbations grows up to an upper bound as time tends to infinity, occurs in the range of typical, moderate values of the concerning hydraulic parameters. From the

nonlinear analysis, we found reasonable agreement between predicted and experimental results for the lateral distribution of the time-averaged flow velocity, lateral kinematic eddy viscosity, shear layer width and maximum friction velocity in the fully developed stage of the perturbations.

Contents

List of Figures

List of Tables

Chapter 1

Introduction

Parallel shear flows are commonly observed either in geophysical flows, e.g. flows in compound channels, flows in channels with lateral varying bottom roughness, flows in channel containing lateral vegetation, as well as in engineered flows, such as flows adjacent to foams, filters and packed beds (Ikeda et al. (1994), White and Nepf (2007)). The lateral velocity gradient may induce flow instability and the generation of large-scale horizontal vortices, which have a strong influence on the velocity distribution and the flow discharge of a channel. Though various studies on instability in channels with lateral velocity gradients have been performed, only theoretical studies are reviewed herein.

Tamai et al. (1986) observed the generation of large eddies on the water surface in a set of experiments with compound channels consisting of a main channel and a flood plain. They concluded that the shear layer in the lateral velocity profile around the interface between the main channel and the flood plain is the predominant cause for the generation of large eddies. They applied the stability analysis of Michalke (1964) with the use of the Rayleigh stability equation to their experimental results, and found that their observations were able to be explained by the analysis.

Chu et al. (1991) performed a linear stability analysis of shear flows in channels with varying flow depths and varying bottom roughness. They employed the St. Venant shallow water equations with the free water surface approximated by a rigid lid, which is a valid simplification when the Froude number is close to zero. The perturbation equations reduced to a modified Rayleigh equation, which can be relatively easily solved. Because it is not

possible to reproduce the lateral gradient of the streamwise velocity without including the Reynolds stress in their formulation, they adopted an assumption that the flow depth and the bottom roughness vary gradually across the channel in order to approximate it. They found that flow stabilizes when the bottom roughness is sufficiently large, and the lateral variation of flow is sufficiently small.

Ikeda et al. (1994) performed a temporal linear stability analysis of a partially vegetated channel. They obtained the base state flow with the use of the St. Venant shallow water equations including the Reynolds stress expressed by the lateral kinematic eddy viscosity empirically determined in experiments. In the perturbed problem, however, they ignored the Reynolds stress and the variation of the water surface elevation, in effect reducing their perturbed equations to a modified Rayleigh equation again. They found that the dimensional angular frequency of maximum instability is uniquely correlated with the ratio of two velocities a sufficient distance from the boundary between the non-vegetated and vegetated zones.

Ghidaoui and Kolyshkin (1999) performed a temporal linear stability analysis of a channel flow with lateral velocity gradients without the rigid-lid assumption. The Reynolds stress was included in their formulation by means of the eddy viscosity term of Chen and Jirka (1997). Semi-empirical expressions were used to describe the base flow profile, containing regression parameters which were not correlated to a specific flow field (i.e., the source of flow retardation in part of the channel was not specified). Their computations showed that the influence of the Reynolds number, defined using the eddy viscosity, on the stability domain is small when it surpasses 1000.

Prooijen and Uijttewaal (2002) have also included the turbulent viscosity as in Chen and Jirka (1997) in their temporal and spatial linear stability analysis of a channel flow with a lateral velocity gradient generated by two separate water supplies with different velocities. The mean flow field, which varied along the streamwise direction, was assumed to be the base state and the rigid-lid assumption was employed, which is a reasonable simplification, given that the Froude number in their experimental runs did not exceed 0.5.

White and Nepf (2007) performed a complete set of experiments and a spatial stability analysis of a channel partially obstructed by an array of circular cylinders by the use of the

modified Rayleigh equations following Chu et al. (1991), with the Reynolds stress scaled with the width of the shear layer around the edge of the array. They made use of the rigid-lid assumption, in accordance with the condition of small Froude numbers met in their experiments (always below 0.25). They concluded that even though the drag differential of the vegetated zone reinforces shear instability, the overall drag damps it if the background friction in the channel is sufficiently large, thus allowing a range of stability characteristics.

In this study, we perform a temporal linear stability analysis of flow in an open channel partially covered with vegetation. By not employing the rigid-lid and the inviscid flow assumptions, we could study the effects of the Froude number and the kinematic eddy viscosity, respectively, on the growth rate of perturbations. We employ the St. Venant shallow water equations with the Reynolds stress included to reproduce the velocity gradient due to the differential drag between the regions with and without vegetation. The temporal and spatial variations of flow vanish except for the lateral variation of the streamwise velocity in the base state, which is used as a starting point of the stability analysis. This base state flow field is not, however, just a temporal average of flow affected by fully-developed horizontal vortices, but the flow undisturbed by the vortices. We thus employ a kinematic eddy viscosity representing turbulence with a length scale smaller than the flow depth. Differently from Chen and Jirka (1997), the eddy viscosity employed herein is estimated for the flow unaffected by the large-scale horizontal vortices. We impose perturbations on the base state flow velocities and flow depth, and study how various hydraulic parameters affect the time development of the perturbations.

The predictive theory of the present study also included a weakly nonlinear stability analysis. The term weakly herein means that the time variation of the amplitude is much slower than the time variation of the wavelike part of the disturbance. We made use of the multiple scale analysis, a perturbation technique where the neutral instability, i.e., the condition where the growth rate of the perturbations is zero, is deviated towards the unstable region, i.e., where the perturbation grows with time. The bifurcation pattern was found to be typically supercritical, where the absolute value of the amplitude reaches an equilibrium condition as time tends to infinity. The theory was able to predict the eddy viscosity corresponding to the large-scale lateral motions.

Chapter 2

Formulation

Suppose that water is flowing through a wide rectangular open-channel with lateral emergent rigid vegetation (trees) as shown in Fig. 2-1. The vegetation is modeled by an array of regularly spaced cylinders with a uniform diameter installed only on one side of the channel. The model of cylinders as vegetation employed herein has been widely used in previous studies (e.g., Ikeda et al. (1991), Tsujimoto (1991), Tsujimoto and Kitamura (1992), Ikeda et al. (1994), Xiaohui and Li (2002) and White and Nepf (2007)). The region of the channel covered with vegetation is defined as the 'vegetated zone', the width of which is denoted by $\tilde{B}_v$. The region of the channel without vegetation is defined as the 'non-vegetated zone', the width of which is denoted by $\tilde{B}$.

2.1 Governing equations

In this study, we focus on horizontal vortices generated in the shallow flow in a wide rectangular open channel. The horizontal length scale of the vortices is commonly large compared with the scale of the flow depth. The generation of such thin vortices can be described by the depth-averaged shallow water formulation. In particular, the momentum equations employed in this analysis need to include the Reynolds stress and the drag force due to vegetation in order to represent the lateral velocity distribution due to the differential drag between the non-vegetated and vegetated zones. The momentum equations in the stream-

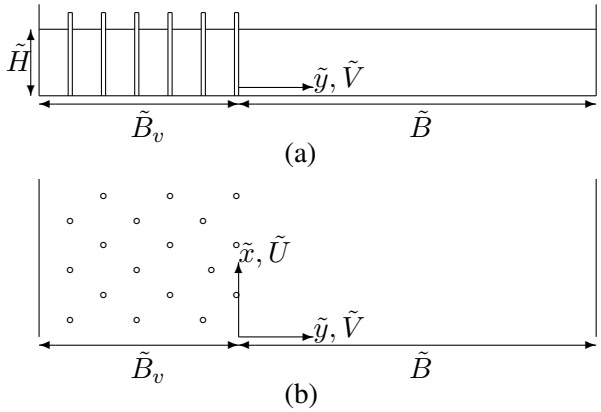

Figure 2-1: Conceptual diagram of the channel with vegetation. (a) The cross-sectional view, and (b) the plan view.

wise and transverse directions ($\tilde{x}$ and $\tilde{y}$) and the continuity equation are

$$\frac{\partial \tilde{U}}{\partial \tilde{t}} + \tilde{U}\frac{\partial \tilde{U}}{\partial \tilde{x}} + \tilde{V}\frac{\partial \tilde{U}}{\partial \tilde{y}} = gS - g\frac{\partial \tilde{H}}{\partial \tilde{x}} - \frac{\tilde{T}_{bx} + \tilde{D}_x}{\rho \tilde{H}} + \frac{1}{\rho}\left(\frac{\partial \tilde{T}_{xx}}{\partial \tilde{x}} + \frac{\partial \tilde{T}_{xy}}{\partial \tilde{y}}\right), \quad (2.1a)$$

$$\frac{\partial \tilde{V}}{\partial \tilde{t}} + \tilde{U}\frac{\partial \tilde{V}}{\partial \tilde{x}} + \tilde{V}\frac{\partial \tilde{V}}{\partial \tilde{y}} = -g\frac{\partial \tilde{H}}{\partial \tilde{y}} - \frac{\tilde{T}_{by} + \tilde{D}_y}{\rho \tilde{H}} + \frac{1}{\rho}\left(\frac{\partial \tilde{T}_{yx}}{\partial \tilde{x}} + \frac{\partial \tilde{T}_{yy}}{\partial \tilde{y}}\right), \quad (2.1b)$$

$$\frac{\partial \tilde{H}}{\partial \tilde{t}} + \frac{\partial \tilde{U}\tilde{H}}{\partial \tilde{x}} + \frac{\partial \tilde{V}\tilde{H}}{\partial \tilde{y}} = 0, \quad (2.1c)$$

where $\tilde{t}$ is time, $\tilde{x}$ is the streamwise coordinate, $\tilde{y}$ is the lateral coordinate, the origin of which is taken at the interface between the vegetated and non-vegetated zones, $\tilde{U}$ and $\tilde{V}$ are the $\tilde{x}$ and $\tilde{y}$ components of the flow velocity respectively, $\tilde{H}$ is the flow depth, $\tilde{T}_{bx}$ and $\tilde{T}_{by}$ are the $\tilde{x}$ and $\tilde{y}$ components of the bed shear stress respectively, $\tilde{D}_x$ and $\tilde{D}_y$ are the $\tilde{x}$ and $\tilde{y}$ components of the drag force due to vegetation respectively, $\tilde{T}_{ij}$ $(i, j = x, y)$ is the Reynolds stress tensor, ρ is the density of water, g is the gravity acceleration, and S is the bed slope of the channel. The tilde denotes dimensional variables, which is to be dropped after normalization.

The drag force vector ($\tilde{D}_x$, $\tilde{D}_y$) is described by the expression

$$(\tilde{D}_x, \tilde{D}_y) = \begin{cases} 0 & \text{in the non-vegetated zone,} \\ \dfrac{\rho C_D \tilde{a} \tilde{H}}{2}(\tilde{U}^2 + \tilde{V}^2)^{1/2}(\tilde{U}, \tilde{V}) & \text{in the vegetated zone,} \end{cases} \quad (2.2)$$

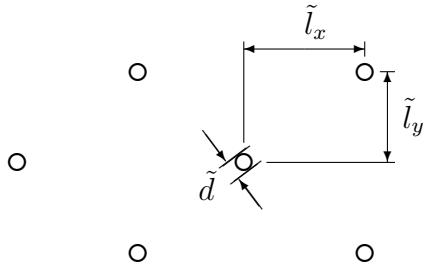

Figure 2-2: The plan view of an array of regularly-spaced cylinders as a model of vegetation.

where C_D is the drag coefficient of vegetation, typically estimated 1 to 2. In addition, $\tilde{a}$ is a parameter describing the density of vegetation, written by

$$\tilde{a} = \frac{\tilde{d}}{\tilde{l}_x \tilde{l}_y}, \tag{2.3}$$

where $\tilde{d}$ is the diameter of cylinders and $\tilde{l}_x$ and $\tilde{l}_y$ are the distances between two adjacent cylinders in the $\tilde{x}$ and $\tilde{y}$ directions respectively, as shown in Fig. 2-2.

The bed shear stress is related to the flow velocity by means of the bed friction coefficient C_f, such that

$$(\tilde{T}_{bx}, \tilde{T}_{by}) = \rho C_f (\tilde{U}^2 + \tilde{V}^2)^{1/2} (\tilde{U}, \tilde{V}). \tag{2.4}$$

Though the bed friction coefficient C_f is a weak function of the flow depth relative to the roughness height, it is assumed to be constant and common in both vegetated and non-vegetated zones for simplicity.

With the use of Boussinesq's kinematic eddy viscosity, the Reynolds stresses are expressed by

$$\tilde{T}_{xx} = 2\rho\tilde{\nu}_T \frac{\partial \tilde{U}}{\partial \tilde{x}}, \tag{2.5a}$$

$$\tilde{T}_{xy} = \tilde{T}_{yx} = \rho\tilde{\nu}_T \left(\frac{\partial \tilde{U}}{\partial \tilde{y}} + \frac{\partial \tilde{V}}{\partial \tilde{x}} \right), \tag{2.5b}$$

$$\tilde{T}_{yy} = 2\rho\tilde{\nu}_T \frac{\partial \tilde{V}}{\partial \tilde{y}}, \tag{2.5c}$$

where $\tilde{\nu}_T$ is the kinematic eddy viscosity. We assume that, in the base state before insta-

bility occurs, the flow is already affected by turbulence the length scale of which is smaller than the flow depth mainly generated by the bottom friction (sub-depth scale turbulence). Therefore, the kinematic eddy viscosity $\tilde{\nu}_T$ should correspond to the sub-depth scale turbulence. As the velocity distribution results from the sub-depth scale turbulence, we employ a logarithmic velocity distribution in the form

$$\frac{\langle \tilde{U} \rangle}{\tilde{U}_f} = \frac{1}{\kappa} \ln \frac{\tilde{z}}{\tilde{k}_s} + K_s, \tag{2.6}$$

where the brackets denote local variables which are not depth-averaged, $\tilde{U}_f$ is the friction velocity ($= \sqrt{\tilde{T}_b/\rho}$), $\tilde{T}_b$ is the bottom shear stress, κ is the Kármán constant ($= 0.4$), $\tilde{z}$ is the coordinate in the depth direction, $\tilde{k}_s$ is the roughness height, and K_s is a constant determined as 8.5 in experiments. The shear stress $\langle \tilde{T}_{xz} \rangle$ is negligibly small at the water surface, increases linearly in the downward depth direction, and reaches the bottom shear stress $\tilde{T}_b$ at the channel bottom, such that

$$\langle \tilde{T}_{xz} \rangle = \rho \tilde{U}_f^2 \left(1 - \frac{\tilde{z}}{\tilde{H}} \right). \tag{2.7}$$

With the use of the local (not depth-averaged) kinematic eddy viscosity, the shear stress $\langle \tilde{T}_{xz} \rangle$ is defined as

$$\langle \tilde{T}_{xz} \rangle = \rho \langle \tilde{\nu}_T \rangle \frac{\mathrm{d}\langle \tilde{U} \rangle}{\mathrm{d}\tilde{z}}. \tag{2.8}$$

Substitution of (2.6) and (2.7) into (2.8) yields

$$\langle \tilde{\nu}_T \rangle = \kappa \tilde{U}_f \tilde{z} \left(1 - \frac{\tilde{z}}{\tilde{H}} \right). \tag{2.9}$$

Taking the average of the above equation from the bottom to the water surface, we obtain

$$\tilde{\nu}_T = \frac{1}{6} \kappa \tilde{U}_f \tilde{H}. \tag{2.10}$$

The formulation described above can be applied to the region sufficiently far from the vegetated zone where there is no influence of vegetation. The kinematic eddy viscosity in

such a region takes the form

$$\tilde{\nu}_T = \frac{1}{6}\kappa \tilde{U}_{f\infty}\tilde{H}_{\infty}. \tag{2.11}$$

where $\tilde{U}_{f\infty}$ and $\tilde{H}_{\infty}$ are the friction velocity and the flow depth in the region sufficiently far from the vegetated zone, respectively. We assume that the sub-depth scale turbulence is rather isotropic. Therefore, the above formulation is expected to describe the Reynolds stresses in the streamwise and lateral directions a sufficient distance from the vegetated zone. Although the kinematic eddy viscosity in the horizontal direction is known to be larger than (2.11), as in Chen and Jirka (1997), we assumed that the increase in the kinematic eddy viscosity is caused by large-scale horizontal vortices generated by instability.

In the shear layer formed around the boundary between the two zones, and inside the vegetated zone, the velocity and the shear velocity are reduced because of the Reynolds stress and the drag force due to vegetation. In addition, the length scale of sub-depth scale vortices may be affected by a typical length scale of vegetation such as the vegetation spacing. According to the experimental results of Ikeda et al. (1991), however, the depth-averaged kinematic eddy viscosity even in the shear layer and the vegetated zone can be represented by (2.11). This may be attributed to the fact that the sum of the resistant forces (the bed shear stress, the Reynolds stress and the vegetation drag force) remains constant regardless of the reduction in the bed shear stress in the shear layer and the vegetated zone. The kinematic eddy viscosity may be correlated to the total resistant force. Furthermore, since the flow depth and the spacing of vegetation in Ikeda et al.'s experiments are both in the same range, the kinematic eddy viscosity in the vegetated zone may not be strongly affected by vegetation. These assumptions and (2.11) are employed in this study as well. Therefore, the Reynolds stress in (2.1a–b) are expressed by the constant sub-depth kinematic eddy viscosity as in (2.11), for both the non-vegetated and vegetated zones.

At the side walls, the velocity vanishes in the directions both tangential and normal to the side walls. The following conditions therefore hold:

$$\tilde{U} = 0 \qquad \text{at} \qquad \tilde{y} = \tilde{B}, -\tilde{B}_v, \tag{2.12a}$$

$$\tilde{V} = 0 \qquad \text{at} \qquad \tilde{y} = \tilde{B}, -\tilde{B}_v. \tag{2.12b}$$

In the shallow water formulation, however, it is not easy to make use of the conditions of vanishing streamwise velocity (2.12a) (non-slip conditions). In place of these conditions, the following slip conditions are often used:

$$\frac{\partial \tilde{U}}{\partial \tilde{y}} = 0 \quad \text{at} \quad \tilde{y} = \tilde{B}, -\tilde{B}_v. \tag{2.13}$$

At a sufficient distance from the boundary between the two zones, the streamwise velocity asymptotically approaches constant velocities in both the non-vegetated and vegetated zones in the base state. If $\tilde{B}$ and $\tilde{B}_v$ are sufficiently large, and the slip condition (2.13) holds, the streamwise velocity is constant at both side walls in the base state, i.e. for which

$$\tilde{U} = \tilde{U}_\infty \quad \text{at} \quad \tilde{y} = \tilde{B}; \quad \tilde{U} = \tilde{U}_{-\infty} \quad \text{at} \quad \tilde{y} = -\tilde{B}_v, \tag{2.14}$$

where $\tilde{U}_\infty$ and $\tilde{U}_{-\infty}$ are the velocities at a sufficient distance from the boundary in the non-vegetated and vegetated zones, respectively. We assume that both side walls are located at a sufficient distance from the boundary, and employ (2.12b) and (2.13) as the boundary conditions at the side walls.

Right at the boundary between the non-vegetated and vegetated zones, the velocities, flow depth and shear stresses are continuous, such that

$$\lim_{\tilde{y}\to+0} \left(\tilde{U}, \tilde{V}, \tilde{H}, \tilde{T}_{xx}, \tilde{T}_{xy}, \tilde{T}_{yy}\right) = \lim_{\tilde{y}\to-0} \left(\tilde{U}, \tilde{V}, \tilde{H}, \tilde{T}_{xx}, \tilde{T}_{xy}, \tilde{T}_{yy}\right). \tag{2.15}$$

2.2 Normalization

At a sufficient distance from the boundary between the two zones in the base state normal flow equilibrium condition, $\tilde{U}$ and $\tilde{H}$ are constant, and $\tilde{V}$ vanishes. Thus, (2.1) allows the solutions

$$\tilde{U}_\infty = \left(\frac{g\tilde{H}_\infty S}{C_f}\right)^{1/2}, \quad \tilde{U}_{-\infty} = \left(\frac{2g\tilde{H}_\infty S}{2C_f + C_D\tilde{a}\tilde{H}_\infty}\right)^{1/2}. \tag{2.16}$$

The velocity and flow depth at a sufficient distance from the vegetated zone, $\tilde{U}_\infty$ and $\tilde{H}_\infty$, are used for the normalization. The velocities and flow depth are then rendered dimension-

less according to the following expressions:

$$(\tilde{U}, \tilde{V}) = \tilde{U}_\infty (U, V), \quad \tilde{H} = \tilde{H}_\infty H. \tag{2.17}$$

The independent variables $\tilde{x}$, $\tilde{y}$ and $\tilde{t}$ are normalized with the use of the width of the non-vegetated zone $\tilde{B}$, such that

$$(\tilde{x}, \tilde{y}) = \tilde{B}(x, y), \quad \tilde{t} = \frac{\tilde{B}}{\tilde{U}_\infty} t. \tag{2.18}$$

With the use of the above normalization, the governing equations (2.1) are rewritten in the form

$$\frac{\partial U}{\partial t} + U\frac{\partial U}{\partial x} + V\frac{\partial U}{\partial y} = -F^{-2}\frac{\partial H}{\partial x} + \beta\left(1 - \frac{T_{bx} + D_x}{H}\right) + \epsilon\left(\frac{\partial^2 U}{\partial x^2} + \frac{\partial^2 U}{\partial y^2}\right), \tag{2.19a}$$

$$\frac{\partial V}{\partial t} + U\frac{\partial V}{\partial x} + V\frac{\partial V}{\partial y} = -F^{-2}\frac{\partial H}{\partial y} - \beta\frac{T_{by} + D_y}{H} + \epsilon\left(\frac{\partial^2 V}{\partial x^2} + \frac{\partial^2 V}{\partial y^2}\right), \tag{2.19b}$$

$$\frac{\partial H}{\partial t} + \frac{\partial UH}{\partial x} + \frac{\partial VH}{\partial y} = 0, \tag{2.19c}$$

where (T_{bx}, T_{by}) and (D_x, D_y) are the normalized bed shear stress and vegetation drag vectors, respectively, written in the form

$$(T_{bx}, T_{by}) = \left(U^2 + V^2\right)^{1/2} (U, V), \tag{2.19d}$$

$$(D_x, D_y) = \begin{cases} \alpha \left(U^2 + V^2\right)^{1/2} H (U, V) & \text{if} \quad -B_v \le y \le 0, \\ 0 & \text{if} \quad 0 \le y \le 1, \end{cases} \tag{2.19e}$$

where the range $-B_v \le y \le 0$ corresponds to the vegetated zone and the range $0 \le y \le 1$ corresponds to the non-vegetated zone. The above normalized governing equations include the four non-dimensional parameters β, ϵ, F and α. The parameter β, which expresses the relative importance of the bed shear effect, is dependent on the aspect ratio of the non-

vegetated zone $A_R = \tilde{B}/\tilde{H}_\infty$, and the bottom friction coefficient C_f, such that

$$\beta = \frac{C_f \tilde{B}}{\tilde{H}_\infty} = C_f A_R. \tag{2.20}$$

The parameter ϵ is associated with the eddy viscosity $\tilde{\nu}_T$, expressed by (2.11), in the form

$$\epsilon = \frac{\tilde{\nu}_T}{\tilde{U}_\infty \tilde{B}} = \frac{C_f^{1/2} \tilde{H}_\infty}{15\tilde{B}} = \frac{C_f^{1/2}}{15 A_R}. \tag{2.21}$$

The Froude number F is given by

$$F = \frac{\tilde{U}_\infty}{\sqrt{\tilde{g}\tilde{H}_\infty}} = \left(\frac{S}{C_f}\right)^{1/2}. \tag{2.22}$$

The parameter α is related to the vegetation drag and density, and is defined by

$$\alpha = \frac{C_D \tilde{a} \tilde{H}_\infty}{2C_f}. \tag{2.23}$$

Chapter 3

Base state normal flow

In the base state, (2.19) reduces to

$$\beta\left(1-U_0^2\right)+\epsilon\frac{\mathrm{d}^2U_0}{\mathrm{d}y^2}=0 \qquad \text{if} \qquad 0\leq y\leq 1, \tag{3.1a}$$

$$\beta\left[1-U_0^2\left(1+\alpha\right)\right]+\epsilon\frac{\mathrm{d}^2U_0}{\mathrm{d}y^2}=0 \qquad \text{if} \qquad -B_v\leq y\leq 0, \tag{3.1b}$$

where U_0 is the streamwise velocity in the base state, which is a function only of the transverse coordinate y.

The normalization of ($\tilde{U}_\infty$, $\tilde{U}_{-\infty}$) leads to (1, ϕ), where ϕ is the ratio between the undisturbed velocities in the vegetated and non-vegetated zones at a sufficient distance from their boundary, which is related to the non-dimensional parameter α, such that

$$\phi=\frac{\tilde{U}_{-\infty}}{\tilde{U}_\infty}=\frac{1}{\left(1+\alpha\right)^{1/2}}. \tag{3.2}$$

The domain of ϕ is $0<\phi\leq 1$; ϕ approaches to 0 when the vegetation obstructs the flow completely in the vegetated zone ($\alpha\to\infty$), and takes the value of unity when there is no vegetation ($\alpha=0$). The boundary conditions corresponding to (2.13) and (2.14) in the base state are then

$$\frac{\mathrm{d}U_0}{dy}=0 \quad \text{at} \quad \tilde{y}=1,-B_v, \tag{3.3a}$$

$$U=1 \quad \text{at} \quad y=1, \quad U=\phi \quad \text{at} \quad y=-B_v. \tag{3.3b}$$

And the matching conditions (2.15) reduce to

$$\lim_{y\to+0} U_0 = \lim_{y\to-0} U_0 = \psi, \tag{3.4a}$$

$$\lim_{y\to+0} \frac{\mathrm{d}U_0}{\mathrm{d}y} = \lim_{y\to-0} \frac{\mathrm{d}U_0}{\mathrm{d}y}, \tag{3.4b}$$

where ψ is the base flow velocity between the non-vegetated and vegetated zones.

3.1 Explicit analytical solutions of the base state

3.1.1 Non-vegetated zone

In order to obtain an explicit analytical solution for (3.1a), we start by multiplying this equation by $\mathrm{d}U_0/\mathrm{d}y$:

$$\beta\frac{\mathrm{d}U_0}{\mathrm{d}y} - \beta U_0^2\frac{\mathrm{d}U_0}{\mathrm{d}y} + \epsilon\frac{\mathrm{d}U_0}{\mathrm{d}y}\frac{\mathrm{d}^2U_0}{\mathrm{d}y^2} = 0 \tag{3.5}$$

Integration of (3.5) with respect to y leads to

$$\beta U_0 - \frac{\beta}{3}U_0^3 + \frac{\epsilon}{2}\left(\frac{\mathrm{d}U_0}{\mathrm{d}y}\right)^2 = C_0, \tag{3.6}$$

where C_0 is an integral constant which is determined by introducing the boundary conditions (3.3) into (3.6). We then obtain

$$C_0 = \frac{2\beta}{3}. \tag{3.7}$$

Substituting (3.7) into (3.6) and writing the resulting equation in integral form, we have

$$\left(\frac{3\epsilon}{2\beta}\right)^{1/2}\int_{\psi}^{U_0}\frac{\mathrm{d}U_0}{(1-U_0)(U_0+2)^{1/2}} = \int_0^y \mathrm{d}y = y. \tag{3.8}$$

We introduce the following variable transformation:

$$(U_0+2)^{1/2} = \chi. \tag{3.9}$$

By employing the above transformation, (3.8) is rewritten as

$$\left(\frac{3\epsilon}{2\beta}\right)^{1/2}\int_{\chi_\psi}^{\chi}\frac{2\mathrm{d}\chi}{(3-\chi^2)}=y, \tag{3.10}$$

where χ_ψ is the value of χ which corresponds to ψ,

$$\chi_\psi=(\psi+2)^{1/2}. \tag{3.11}$$

Another variable transformation is introduced,

$$\chi=\sqrt{3}\tanh\gamma. \tag{3.12}$$

By employing the above transformation, (3.10) is rewritten as

$$\left(\frac{2\epsilon}{\beta}\right)^{1/2}\int_{\gamma_\psi}^{\gamma}\mathrm{d}\gamma=\left(\frac{2\epsilon}{\beta}\right)^{1/2}(\gamma-\gamma_\psi)=y, \tag{3.13}$$

where γ_ψ is the value of γ which corresponds to χ_ψ,

$$\gamma_\psi=\tanh^{-1}\left(\frac{\chi_\psi}{\sqrt{3}}\right)=\tanh^{-1}\left(\frac{\psi+2}{3}\right)^{1/2}. \tag{3.14}$$

The variable γ is related to U_0 by $U_0=3\tanh^2\gamma-2$. Thus, we have

$$U_0=3\tanh^2\left[\left(\frac{\beta}{2\epsilon}\right)^{1/2}y+\tanh^{-1}\left(\frac{\psi+2}{3}\right)^{1/2}\right]-2. \tag{3.15}$$

3.1.2 Vegetated zone

Similarly to the non-vegetated zone, we multiply (3.1b) by $\mathrm{d}U_0/\mathrm{d}y$:

$$\beta\frac{\mathrm{d}U_0}{\mathrm{d}y}-\beta(1-\alpha)U_0^2\frac{\mathrm{d}U_0}{\mathrm{d}y}+\epsilon\frac{\mathrm{d}U_0}{\mathrm{d}y}\frac{\mathrm{d}^2U_0}{\mathrm{d}y^2}=0. \tag{3.16}$$

By integrating the above with respect to y, we have

$$\beta U_0 - \frac{\beta}{3}(1-\alpha)U_0^3 + \frac{\epsilon}{2}\left(\frac{\mathrm{d}U_0}{\mathrm{d}y}\right)^2 = C_1, \tag{3.17}$$

where the integral constant C_1 is determined by introducing the boundary conditions (3.3) into (3.17),

$$C_1 = \frac{2\beta\phi}{3}. \tag{3.18}$$

Substituting (3.18) into (3.17) and writing the resulting equation in integral form, we have

$$\left(\frac{3\epsilon}{2\beta}\right)^{1/2} \int_{\psi}^{U_0} \frac{\phi \mathrm{d}U_0}{(U_0-\phi)(U_0+2\phi)^{1/2}} = \int_0^y \mathrm{d}y = y. \tag{3.19}$$

We introduce the following variable transformation:

$$(U_0 + 2\phi)^{1/2} = \lambda. \tag{3.20}$$

By employing the above transformation, (3.19) is rewritten as

$$\left(\frac{3\epsilon}{2\beta}\right)^{1/2} \int_{\lambda_\psi}^{\lambda} \frac{2\phi \mathrm{d}\lambda}{(\lambda^2 - 3\phi)} = y, \tag{3.21}$$

where λ_ψ is the value of λ corresponding to ψ,

$$\lambda_\psi = (\psi + 2\phi)^{1/2}. \tag{3.22}$$

We employ another variable transformation,

$$\lambda = \sqrt{3\phi}\coth\theta. \tag{3.23}$$

By employing the above transformation, (3.21) is rewritten as

$$\left(\frac{2\epsilon\phi}{\beta}\right)^{1/2} \int_{\theta_\psi}^{\theta} d\theta = \left(\frac{2\epsilon\phi}{\beta}\right)^{1/2} (\theta - \theta_\psi) = -y, \tag{3.24}$$

where θ_ψ is given by

$$\theta_\psi = \coth^{-1}\left(\frac{\lambda_\psi}{\sqrt{3\phi}}\right) = \coth^{-1}\left(\frac{\psi+2\phi}{3\phi}\right)^{1/2}. \tag{3.25}$$

The variable θ is related to U_0 by $U_0 = 3\phi\coth^2\theta - 2\phi$. Thus, we have

$$U_0 = 3\phi\coth^2\left[-\left(\frac{\beta}{2\epsilon\phi}\right)^{1/2} y + \coth^{-1}\left(\frac{\psi+2\phi}{3\phi}\right)^{1/2}\right] - 2\phi. \tag{3.26}$$

3.1.3 Velocity at the boundary between the two zones

With the use of (3.15) and (3.26), the matching condition (3.4b) is rewritten in the form

$$(\phi+1)(\phi-1)\psi^3 - 2\phi^2(\phi-1) = 0. \tag{3.27}$$

Because $\phi \neq 1$, the above equation is reduced to

$$\psi = \left(\frac{2\phi^2}{1+\phi}\right)^{1/3}. \tag{3.28}$$

3.2 Results

Rewriting the base state explicit analytical solutions (3.15) and (3.26), we have

$$U_0(y) = \begin{cases} 3\tanh^2\left[\left(\dfrac{\beta}{2\epsilon}\right)^{1/2} y + \tanh^{-1}\left(\dfrac{\psi+2}{3}\right)^{1/2}\right] - 2 & \text{if} \quad 0 \le y \le 1, \\ 3\phi\coth^2\left[-\left(\dfrac{\beta}{2\epsilon\phi}\right)^{1/2} y + \coth^{-1}\left(\dfrac{\psi+2\phi}{3\phi}\right)^{1/2}\right] - 2\phi & \text{if} \quad -B_v \le y \le 0. \end{cases} \tag{3.29}$$

The streamwise velocity in the base state, U_0, is thus found to be expressed by hyperbolic-tangent and hyperbolic-cotangent functions which are invariant in time and in the streamwise direction, and include four non-dimensional parameters β, ϵ, ψ and ϕ, where the later two can be expressed as functions of α, only.

Figs. 3-1(a), (b) and (c) depict the lateral distribution of U_0 as in (3.29) as functions

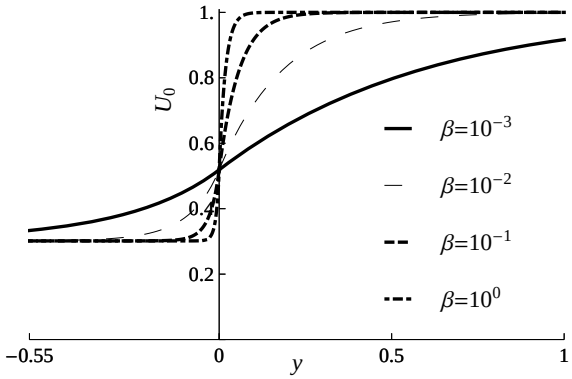

(a)

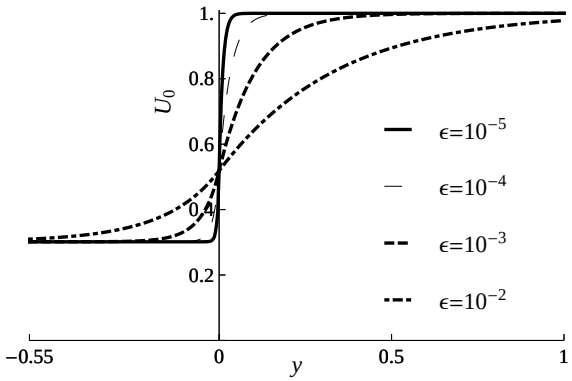

(b)

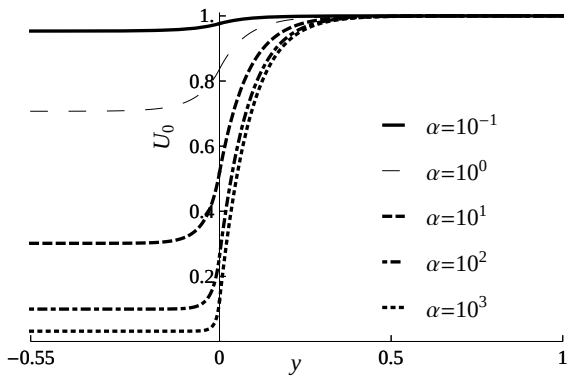

(c)

Figure 3-1: The lateral distribution of the streamwise velocity in the base state U_0 as functions of (a) β for the case $\epsilon = 6 \times 10^{-4}$, $\alpha = 10$, (b) ϵ for the case $\beta = 0.05$, $\alpha = 10$, and (c) α for the case $\beta = 0.05$, $\epsilon = 6 \times 10^{-4}$.

of the parameters β, ϵ and α, respectively. Note that the velocities at the far right and left correspond to $\tilde{U}_\infty$ and $\tilde{U}_{-\infty}$, and the value of U_0 at the far left is ϕ. It is found from Fig. 3-1(a) that, as β increases, the width of the shear layer decreases. This is because an increase in β implies an increase in the relative significance of the bed friction over the vegetation drag. In Fig. 3-1(b), on the other side, the increase of ϵ results in the increase of the shear layer width following the increase of the relative importance of the sub-depth kinematic eddy viscosity. The relative increase of the viscous effects will result in a milder base state velocity gradient. According to Fig. 3-1(c), ϕ decreases with increasing α, as it is natural that the velocity difference between the two zones increases with the vegetation drag parameter. In contrast to β and ϵ, the shear layer width does not strongly depend on α.

Chapter 4

Linear stability analysis

A temporal linear stability analysis is performed herein. A disturbance undulating in the streamwise direction is introduced to the base state. The streamwise and lateral velocities U and V, and the flow depth H are then expanded in the form

$$U(x,y,t) = U_0(y) + AU_1(y)\mathrm{e}^{\mathrm{i}(kx-\omega t)}, \tag{4.1a}$$

$$V(x,y,t) = AV_1(y)\mathrm{e}^{\mathrm{i}(kx-\omega t)}, \tag{4.1b}$$

$$H(x,y,t) = 1 + AH_1(y)\mathrm{e}^{\mathrm{i}(kx-\omega t)}, \tag{4.1c}$$

where A, k and ω are the amplitude, wavenumber and angular frequency of perturbation. In the scheme of temporal linear stability analysis, k is real while ω is complex such that $\omega = \omega_r + \mathrm{i}\Omega$, where ω_r is the real angular frequency and Ω is the growth rate of perturbation.

Substituting (4.1) into the governing equations (2.19), we obtain the following perturbed equations in the non-vegetated zone:

$$\left[\mathrm{i}\left(kU_0-\omega\right) + k^2\epsilon + 2\beta U_0 - \epsilon\frac{\mathrm{d}^2}{\mathrm{d}y^2}\right]U_1 + \frac{\mathrm{d}U_0}{\mathrm{d}y}V_1 + \left(\mathrm{i}kF^{-2} - \beta U_0^2\right)H_1 = 0, \tag{4.2a}$$

$$\left[\mathrm{i}\left(kU_0-\omega\right) + k^2\epsilon + \beta U_0 - \epsilon\frac{\mathrm{d}^2}{\mathrm{d}y^2}\right]V_1 + F^{-2}\frac{\mathrm{d}H_1}{\mathrm{d}y} = 0, \tag{4.2b}$$

$$\mathrm{i}kU_1 + \frac{\mathrm{d}V_1}{\mathrm{d}y} - \mathrm{i}(\omega - kU_0)H_1 = 0. \tag{4.2c}$$

In the vegetated zone, (2.19) becomes

$$\left[\mathrm{i}\left(kU_0-\omega\right)+k^2\epsilon+2\beta U_0\left(1+\alpha\right)-\epsilon\frac{\mathrm{d}^2}{\mathrm{d}y^2}\right]U_1+\frac{\mathrm{d}U_0}{\mathrm{d}y}V_1+\left(\mathrm{i}kF^{-2}-\beta U_0^2\right)H_1=0, \tag{4.3a}$$

$$\left[\mathrm{i}\left(kU_0-\omega\right)+k^2\epsilon+\beta U_0\left(1+\alpha\right)-\epsilon\frac{\mathrm{d}^2}{\mathrm{d}y^2}\right]V_1+F^{-2}\frac{\mathrm{d}H_1}{\mathrm{d}y}=0, \tag{4.3b}$$

$$\mathrm{i}kU_1+\frac{\mathrm{d}V_1}{\mathrm{d}y}-\mathrm{i}\left(\omega-kU_0\right)H_1=0. \tag{4.3c}$$

Since the amplitude of the perturbation A is assumed to be infinitesimally small, the terms containing A^2 have been dropped in the linear stability analysis, so that the results of the analysis are valid only in the range of small amplitudes.

The boundary conditions of vanishing lateral velocity (2.12b) and vanishing shear stress (2.13) at the side walls take the following forms at $O(A)$:

$$\frac{\mathrm{d}U_1}{\mathrm{d}y}=0 \qquad \text{at} \qquad y=-B_v,1, \tag{4.4a}$$

$$V_1=0 \qquad \text{at} \qquad y=-B_v,1. \tag{4.4b}$$

At the interface between the vegetated and non-vegetated zones $y=0$, the matching conditions reduce to

$$\lim_{y\to+0}\left(U_1,V_1,H_1,\frac{\mathrm{d}U_1}{\mathrm{d}y},\frac{\mathrm{d}V_1}{\mathrm{d}y}\right)=\lim_{y\to-0}\left(U_1,V_1,H_1,\frac{\mathrm{d}U_1}{\mathrm{d}y},\frac{\mathrm{d}V_1}{\mathrm{d}y}\right). \tag{4.5}$$

Although there are five matching conditions in (4.5), only four of them are independent since, if four of them are imposed, the other condition is automatically satisfied. Thus, one of these conditions can be dropped afterwards.

A numerical scheme is necessary to solve (4.2) and (4.3) under the boundary and matching conditions (4.4) and (4.5), as the equations obviously do not admit analytical solutions. We employ a spectral collocation method with the Chebyshev polynomials. In the non-

vegetated zone ($0 \leq y \leq 1$), the variables U_1, V_1 and H_1 are expanded in the form

$$U_1 = \sum_{j=0}^{N} a_j T_j(\xi), \quad V_1 = \sum_{j=0}^{N} a_{(N+1)+j} T_j(\xi), \quad H_1 = \sum_{j=0}^{N} a_{2(N+1)+j} T_j(\xi), \tag{4.6a, b, c}$$

and, in the vegetated zone ($-B_v \leq y \leq 0$), they are expanded in the form

$$U_1 = \sum_{j=0}^{N} a_{3(N+1)+j} T_j(\eta), \quad V_1 = \sum_{j=0}^{N} a_{4(N+1)+j} T_j(\eta), \quad H_1 = \sum_{j=0}^{N} a_{5(N+1)+j} T_j(\eta), \tag{4.7a, b, c}$$

where a_j ($j = 0, 1, 2, ..., 6N + 5$) are the coefficients of the Chebyshev polynomials, and $T_j(\xi)$ and $T_j(\eta)$ are the Chebyshev polynomials in ξ and η of degree j. The independent variables ξ and η both range from -1 to 1, and are related to y by the equations $\xi = 2y - 1$ ($0 \leq y \leq 1$) and $\eta = 2y/B_v + 1$ ($-B_v \leq y \leq 0$), respectively. The expansions (4.6) and (4.7) are substituted into the governing equations (4.2) and (4.3) respectively, and the resulting six equations are evaluated at the Gauss-Lobatto points defined by

$$\xi_m = \cos\frac{m\pi}{N}, \quad \eta_m = \cos\frac{m\pi}{N}, \tag{4.8a, b}$$

where $m = 0, 1, ..., N$. Therefore, the number of points where the governing equations are evaluated is $N + 1$. We obtain a system of $6(N + 1)$ algebraic equations with $6(N + 1)$ unknown coefficients $a_0, a_1, a_2, ..., a_{6N+5}$. Eight equations of the system are then replaced by the four boundary conditions (4.4) and four of the matching conditions (4.5). The resulting linear algebraic system can be written in the form

$$\mathcal{M} \begin{bmatrix} a_0 \\ a_1 \\ \vdots \\ a_{6N+5} \end{bmatrix} = 0, \tag{4.9}$$

where $\mathcal{M}$ is a $6(N + 1) \times 6(N + 1)$ matrix in which the elements consist of the coefficients of U_1, V_1 and H_1 in the governing equations (4.2) and (4.3), and the boundary and matching

conditions (4.4) and (4.5). The condition for (4.9) to have a non-trivial solution is that $\mathcal{M}$ should be singular. Thus,

$$|\mathcal{M}| = 0. \tag{4.10}$$

The solution of the above equation takes the functional form

$$\omega = \omega_r + \mathrm{i}\Omega = \omega\left(k, \beta, \epsilon, \alpha, B_v, F\right). \tag{4.11}$$

Chapter 5

Results and discussion: linear stability analysis

As seen in (4.11), there are six important non-dimensional parameters k, β, ϵ, α, B_v, and F determining the growth rate Ω. The contours of the growth rate Ω on the plane of these parameters are shown in Figs. 5-1–5-5. When Ω is positive, the perturbations grow with time, whereas the perturbations decay until they vanish when Ω is negative. The thick solid lines in the figures indicate the neutral instability curve on which $\Omega = 0$ and the perturbations neither grow nor decay, and divide the planes into stable ($\Omega < 0$) and unstable regions ($\Omega > 0$). In the figures, Ω typically becomes negative in the range of sufficiently small and large values of k, and takes a maximum value between them. It follows that Ω as a function of k commonly possesses a characteristic wavenumber k_m associated with the maximum growth rate Ω_m, implying the selection of a preferential wavelength at the linear level.

The parameters β, ϵ, α, B_v, and F were systematically varied from a base set of numerical values consisting of $\beta = 0.05$, $\epsilon = 6 \times 10^{-4}$, $\alpha = 10$, $B_v = 0.55$ and $F = 0.5$. These values were defined based on typical values of the experiments of Ikeda et al. (1991).

In Fig. 5-1(a), the dependence of Ω on β is studied for the case $\epsilon = 6 \times 10^{-4}$, $\alpha = 10$, $B_v = 0.55$ and $F = 0.5$, following the base set of values for these parameters. The growth rate Ω is maximized when β is around 10^{-1}. As β increases or decreases from this value, the flow becomes less stable, and in the range $\beta \gtrapprox 0.5$, the region of positive

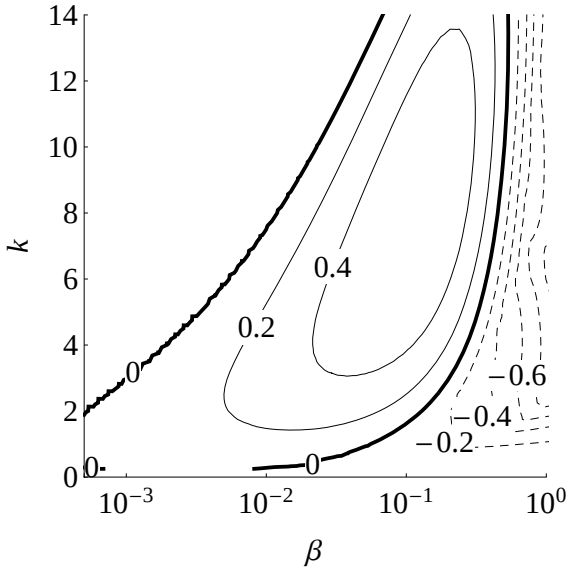

Figure 5-1: The contours of the perturbation growth rate Ω in the β-k plane for the case $\epsilon = 6 \times 10^{-4}$, $\alpha = 10$, $B_v = 0.55$, $F = 0.5$.

Ω completely disappears and the flow becomes stable. In the range of large β, the effect of the bottom friction inhibits the effect of the lateral velocity gradient, as already shown by Chu et al. (1991) and White and Nepf (2007). On the other side, in the range of small β, the relative effect of the small scale turbulences generated by the bottom friction will be reduced, allowing the shear layer to expand further along the transverse direction and leading to a milder lateral gradient of the base state velocity, as in Fig. 3-1(a), leading to the reduction of the growth rate Ω. Although the present shallow water formulation may no longer be valid in the range of $\beta \lessapprox 5 \times 10^{-3}$, the decrease in the growth rate Ω is expected to occur in this range. In the range of sufficiently small β, the shear layer may be affected by the zero disturbance boundary condition of the walls, as pointed by Kolyshkin and Ghidaoui (2002). The range of k for positive Ω and the characteristic wavenumber k_m increase with β. This is because the wavenumber k is normalized by the width of the non-vegetated zone $\tilde{B}$.

The effect of the parameter ϵ on Ω is studied in Fig. 5-2. The parameter ϵ measures the relative effect of the sub-depth kinematic eddy viscosity. Because the sub-depth kinematic eddy viscosity is derived taking into consideration the small scale turbulences generated by the bottom friction before instability takes place, ϵ does not contain the effect of

the large-scale turbulences. It is found from Fig. 5-2 that the flow becomes stable when $\epsilon \gtrapprox 4.0 \times 10^{-3}$. In this range, the dissipation of energy caused by the small scale turbulences will be sufficiently large to suppress the effect of the transverse mixing. On the other side, as ϵ decreases, Ω increases. In the range of very small ϵ, the flow approaches to the inviscid case. The characteristic wavenumber k_m increases with the decrease of ϵ because of the normalization of the wavenumber k. In case we had employed the kinematic eddy viscosity as in Chen and Jirka (1997), the growth rate of perturbations would have been underestimated, following that a larger eddy viscosity would corresponds to a smaller growth rate Ω.

The dependence of Ω on the vegetation drag parameter α is studied in Fig. 5-3. It is found that, in the range of small α, Ω is negative and the flow is stable as already pointed out by Chu et al. (1991) and White and Nepf (2007). As α increases, Ω increases with a slight increase in k_m, which peaks around the point $(\alpha, k) \approx (10^2, 6)$. In the range of $\alpha \gtrapprox 10^2$, Ω decreases with slight decreases in k_m, and Ω becomes negative and the flow becomes stable again when $\alpha \gtrapprox 4 \times 10^3$. In the present analysis, we assume that the kinematic eddy viscosity in the vegetated zone is represented by (2.11) since the typical length scale of vegetation is not significantly smaller than the flow depth. When the vegetation density reaches a certain density, this assumption may no longer be valid. However, it is natural that the flow becomes stable with increasing α since the vegetated zone becomes like a cavity region when α is sufficiently large, and the large-scale horizontal vortices are damped by strong retardation effects. Therefore, the contours of Ω in the range of large α in Fig. 5-3 are at least qualitatively correct.

The effect of the width of the vegetated zone B_v on Ω is shown in Fig. 5-4. It is found from the figure that Ω is negative for any value of k when $B_v \lessapprox 0.1$, and Ω is almost independent of B_v when $B_v \gtrapprox 0.5$. In this analysis, we assume that B_v is large enough that U_0 is almost constant at $y = -B_v$ as described in (2.14). Therefore, Fig. 5-4 is not reliable in the range of small B_v. However, Fig. 5-4 is at least qualitatively correct because the lateral displacement of water is suppressed and the flow becomes stable when B_v is sufficiently small.

The dependence of Ω on the Froude number F is studied in Fig. 5-5. Because the rigid-

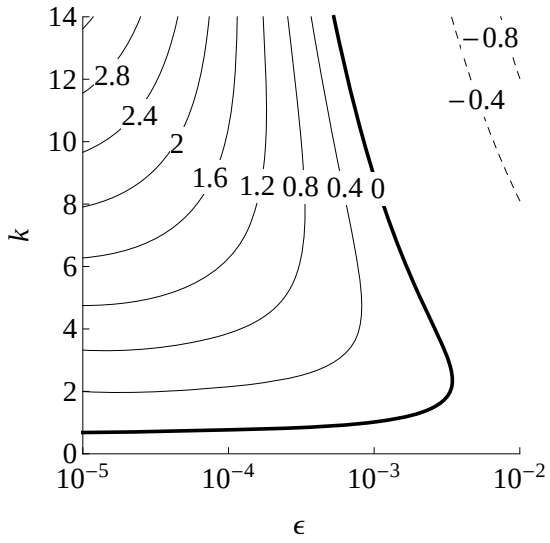

Figure 5-2: The contours of the perturbation growth rate Ω in the ϵ-k plane for the case $\beta = 0.05$, $\alpha = 10$, $B_v = 0.55$, $F = 0.5$.

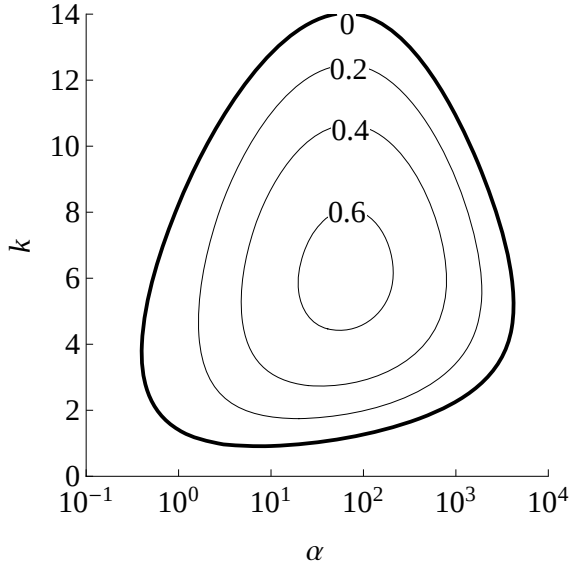

Figure 5-3: The contours of the perturbation growth rate Ω in the α-k plane for the case $\beta = 0.05$, $\epsilon = 6 \times 10^{-4}$, $B_v = 0.55$, $F = 0.5$.

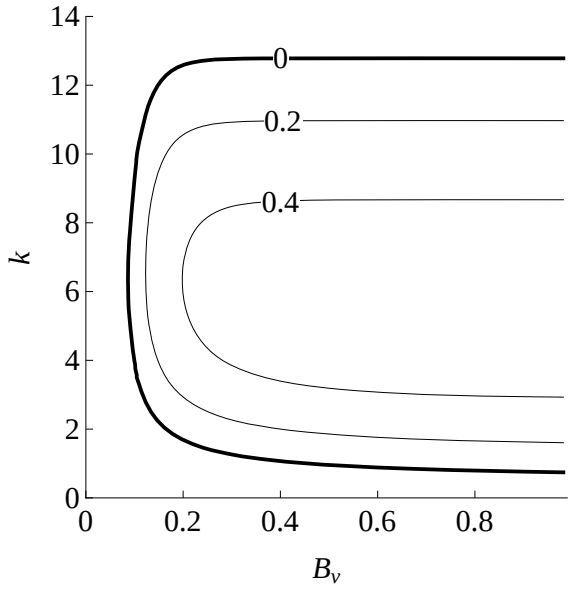

Figure 5-4: The contours of the perturbation growth rate Ω in the B_v-k plane for the case $\beta = 0.05$, $\epsilon = 6 \times 10^{-4}$, $\alpha = 10$, $F = 0.5$.

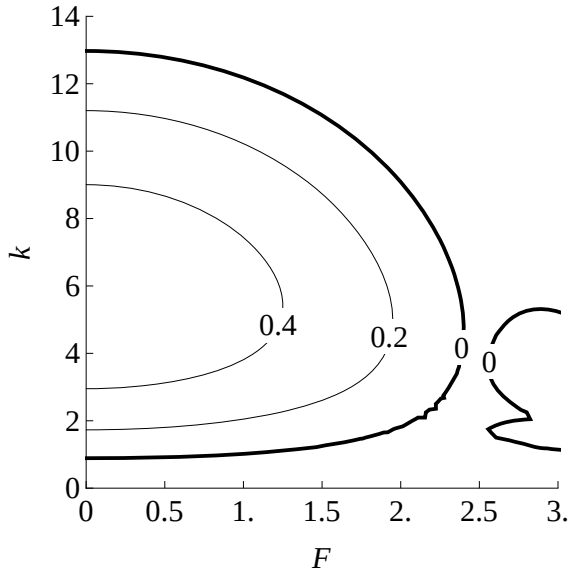

Figure 5-5: The contours of the perturbation growth rate Ω in the F-k plane for the case $\beta = 0.05$, $\epsilon = 6 \times 10^{-4}$, $\alpha = 10$, $B_v = 0.55$.

lid assumption was not employed in the present analysis, the growth rate of perturbations can also be studied for values of F which are not close to zero. It is found from the figure that the flow is unstable in the range of small F. As F increases, the instability weakens and a stable region is observed in the range $F \approx 2.3 - 2.6$. When $F \gtrapprox 2.6$ under the conditions of this figure, the flow is again found to be unstable. It has been empirically known that rapid flow plays stabilizing effects for lateral velocity gradients, which is theoretically explained in this analysis. On the other side, as pointed by Kolyshkin and Ghidaoui (2002), the rapid flow becomes unstable to gravity waves if F is sufficiently large. Therefore, although the flow is found to be stable to the lateral velocity gradients when $F \gtrapprox 2.3$ in Fig. 5-5, it is unstable to gravity when $F \gtrapprox 2.6$.

Fig. 5-6 depicts the neutral instability curves ($\Omega = 0$) for the case $\beta = 0.05$, $\epsilon = 6 \times 10^{-4}$, and $B_v = 0.55$ for varying α and multiple Froude numbers F. The range of small α where the flow is found to be stable when $F = 0.5$ or $F = 1.5$ is more prone to become unstable to gravity, as while the flow is stable when $\alpha \lessapprox 0.5$ for $F = 0.5$ and $F = 1.5$, it becomes unstable to gravity in this range when $F = 2.5$. As F increases from 0.5 to 2.5, the unstable region for $\alpha \gtrapprox 0.5$ diminishes because the gravity effects weaken the instability due to the transverse mixing. The combined effect of rapid flow and lateral mixing stabilizes the flow in the range of $\alpha \approx 10^1$ for $F = 2.5$.

Once the characteristic frequency of the generation of vortices ω_{rm} associated with the maximum growth rate Ω_m is determined, the corresponding time period $\tilde{T}$ can be calculated by the following relation:

$$\tilde{T} = \frac{2\pi \tilde{B}}{\omega_{rm} \tilde{U}_\infty}. \tag{5.1}$$

Assuming that the perturbation with the maximum growth rate Ω_m is realized in experiments and in the field, we compare $\tilde{T}$ predicted in the analysis with the results of the laboratory experiments obtained by Ikeda et al. (1994) and Tsujimoto (1991). In their experiments, vortices were generated by an array of regularly spaced cylinders installed on one side of channels, which is the same setup as assumed in the present analysis. The major hydraulic parameters of the experiments are listed in Table 5.1.

Fig. 5-7 depicts a comparison between the predicted and measured values of $\tilde{T}$. It is

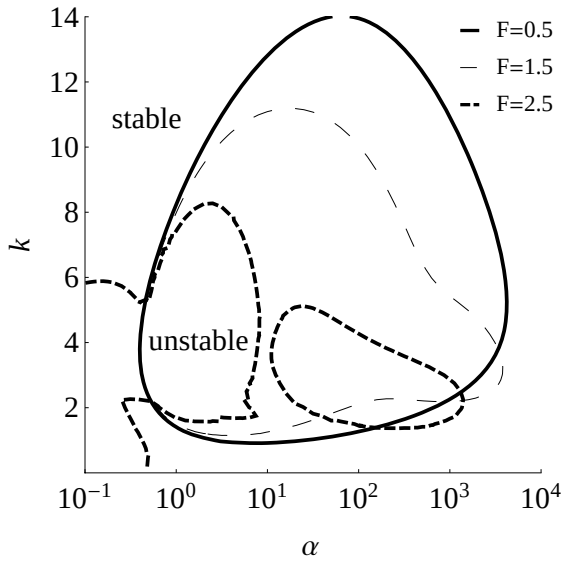

Figure 5-6: The contours of the neutral instability ($\Omega = 0$) in the α-k plane for the case $\beta = 0.05$, $\epsilon = 6 \times 10^{-4}$, $B_v = 0.55$ and multiple Froude numbers F.

Table 5.1: Hydraulic parameters from the experiments of Ikeda et al. (1994) (runs 1–5) and Tsujimoto (1991) (runs IW1–IW3).

Run	β	ϵ ($\times 10^{-4}$)	B_V	F	α	Predicted ω_{rm}	Predicted $\tilde{T}$(s)	Measured $\tilde{T}$(s)
1	0.061	5.19	0.57	0.41	9.9	4.15	2.9	6.4
2	0.061	5.19	0.57	0.75	9.9	4.12	1.6	3.8
5	0.038	6.88	0.57	0.44	15.9	2.63	3.6	9.0
IW1	0.024	4.84	0.43	0.69	67.9	2.64	1.6	3.3
IW2	0.030	5.89	0.43	0.78	50.8	2.70	1.4	2.5
IW3	0.025	5.43	0.43	0.93	63.5	2.54	1.2	1.9

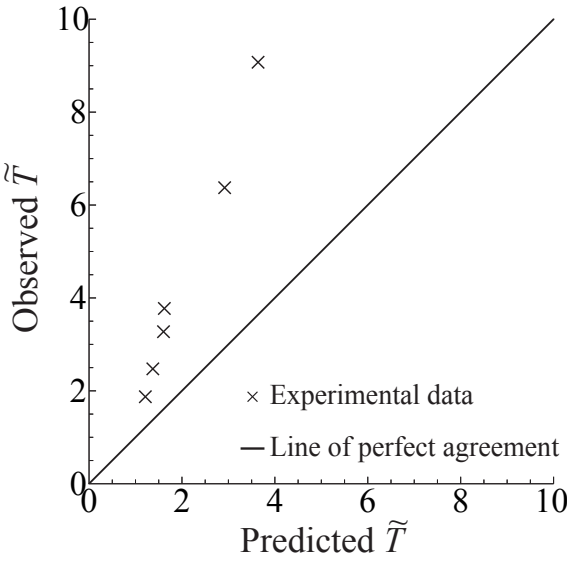

Figure 5-7: Comparison between the predicted and measured periods of the generation of vortices.

found that, though the vortex shedding periods predicted by the present analysis and those observed in the experiments are on the same order of magnitude, the predictions are generally smaller than the observed by a factor of approximately two. The vortex shedding periods observed in the experiments correspond to those in a fully developed stage, which cannot be predicted by the present linear stability analysis. Rather, the results of the linear analysis can reliably reflect only an initial stage of the growth of infinitesimally small disturbances. The vortex shedding period may be longer due to the nonlinear interaction among vortices with a variety of length scales and frequencies.

Ikeda et al. (1994) made a comparison between the vortex shedding periods observed in their experiments and those predicted by their linear stability analysis, and showed good agreement between them. Their analysis employed the lateral kinematic eddy viscosity observed in their experiments which is approximately twice as large as (2.11). The effect of the nonlinear interaction may be attributable to an increase in the mixing efficiency, and is apparently equivalent to the increase in the kinematic eddy viscosity. In order to gain a qualitative understanding of the effect of nonlinear interaction, a weakly nonlinear stability analysis will no doubt prove useful.

Chapter 6

Nonlinear stability analysis

The neutral state obtained from the linear stability analysis is deviated towards the unstable region as

$$\phi = \phi_c - \zeta^2, k = k_c + k_0\zeta^2, \tag{6.1}$$

where ϕ_c is a value of ϕ which lies on the neutral curve, k_c is the preferential wavenumber corresponding to ϕ_c and ζ is the expansion parameter, defined in (6.1). Except for the region where ϕ is sufficiently small, we have that the flow is stable if $\phi < \phi_c$. For this reason, the sign in the expression of the expansion of ϕ is negative. As previously stated, the results in the range of large α, which correspond to a small ϕ, might not be quantitatively reliable. Therefore, this range of neutral stability will not be considered for expansion in the present analysis. The parameter k_0 is introduced to correlate the expansions of ϕ and k.

We perform a weakly analysis, where the time scale of the variation of the amplitude A is much slower than the variation of the wavelike part of the disturbance. The slow time scale t_1 is defined as

$$t = t_0, t_1 = \zeta^2 t. \tag{6.2}$$

From the above relation, the time derivative becomes

$$\frac{\partial}{\partial t} = \frac{\partial}{\partial t_0} + \frac{\partial}{\partial t_1}. \tag{6.3}$$

For simplicity, the subscript 0 is dropped hereafter.

The non-linear interactions of the fundamental wave are generated from the order of A^3. We then expand the velocities and flow depth up to this order in the form

$$U(x,y,t) = U_{0_c}(y) + \zeta\hat{U}_1(x,y,t) + \zeta^2\hat{U}_2(x,y,t) + \zeta^3\hat{U}_3(x,y,t), \tag{6.4a}$$

$$V(x,y,t) = \zeta\hat{V}_1(x,y,t) + \zeta^2\hat{V}_2(x,y,t) + \zeta^3\hat{V}_3(x,y,t), \tag{6.4b}$$

$$H(x,y,t) = 1 + \zeta\hat{H}_1(x,y,t) + \zeta^2\hat{H}_2(x,y,t) + \zeta^3\hat{H}_3(x,y,t), \tag{6.4c}$$

where the circumflex denotes the eigenfunctions in the scheme of nonlinear analysis and U_{0_c} is the base state velocity corresponding to ϕ_c.

6.1 $O(\zeta)$

Substituting (6.1)-(6.4) into (2.19), we obtain the following equations at $O(\zeta)$:

$$G\hat{U}_1 + \frac{\mathrm{d}U_{0_c}}{\mathrm{d}y}\hat{V}_1 + J\hat{H}_1 = 0, \tag{6.5a}$$

$$K\hat{V}_1 + F^{-2}\frac{\partial\hat{H}_1}{\partial y} = 0, \tag{6.5b}$$

$$\frac{\partial\hat{U}_1}{\partial x} + \frac{\partial\hat{V}_1}{\partial y} + P\hat{H}_1 = 0, \tag{6.5c}$$

where the linear operators G, J, K and P are given by the following expressions:

$$G = \begin{cases} \dfrac{\partial}{\partial t} + U_{0_c}\left(2\beta + \dfrac{\partial}{\partial x}\right) - \epsilon\left(\dfrac{\partial^2}{\partial x^2} + \dfrac{\partial^2}{\partial y^2}\right) \text{ if } 0 \le y \le 1, \\ \dfrac{\partial}{\partial t} + U_{0_c}\left(2\beta(1+\alpha_c) + \dfrac{\partial}{\partial x}\right) - \epsilon\left(\dfrac{\partial^2}{\partial x^2} + \dfrac{\partial^2}{\partial y^2}\right) \text{ if } -B_v \le y \le 0, \end{cases} \tag{6.6a}$$

$$J = -\beta U_{0_c}^2 + F^{-2}\frac{\partial}{\partial x}, \tag{6.6b}$$

$$K = \begin{cases} \dfrac{\partial}{\partial t} + U_{0_c}\left(\beta + \dfrac{\partial}{\partial x}\right) - \epsilon\left(\dfrac{\partial^2}{\partial x^2} + \dfrac{\partial^2}{\partial y^2}\right) \text{ if } 0 \le y \le 1, \\ \dfrac{\partial}{\partial t} + U_{0_c}\left(\beta(1+\alpha_c) + \dfrac{\partial}{\partial x}\right) - \epsilon\left(\dfrac{\partial^2}{\partial x^2} + \dfrac{\partial^2}{\partial y^2}\right) \text{ if } -B_v \le y \le 0, \end{cases} \tag{6.6c}$$

$$P = \frac{\partial}{\partial t} + U_{0_c}\frac{\partial}{\partial x}, \tag{6.6d}$$

where α_c is the α corresponding to ϕ_c.

The fundamental perturbations at $O(\zeta)$ are assumed to have a form similar to the one employed in the linear analysis, as follows:

$$\hat{U}_1(x,y,t) = AU_{11}(y)E + \text{c.c.}, \tag{6.7a}$$

$$\hat{V}_1(x,y,t) = AV_{11}(y)E + \text{c.c.}, \tag{6.7b}$$

$$\hat{H}_1(x,y,t) = AH_{11}(y)E + \text{c.c.}, \tag{6.7c}$$

where $E = e^{i(k_c x - \omega_c t)}$, and c.c. is the complex conjugate of the preceding term. Substituting the above expansions into (6.5), we obtain the following equations composed of AE at $O(\zeta)$:

$$G_1 U_{11} + \frac{\mathrm{d}U_{0_c}}{\mathrm{d}y} V_{11} + J_1 H_{11} = 0, \tag{6.8a}$$

$$K_1 V_{11} + F^{-2} \frac{\mathrm{d}H_{11}}{\mathrm{d}y} = 0, \tag{6.8b}$$

$$L_1 U_{11} + \frac{\mathrm{d}V_{11}}{\mathrm{d}y} + P_1 H_{11} = 0. \tag{6.8c}$$

where the linear operators G_n, J_n, K_n, L_n and P_n are given by the following expressions:

$$G_n = \begin{cases} n\mathrm{i}\left(k_c U_{0_c} - \omega_c\right) + 2\beta U_{0_c} + \epsilon(nk_c)^2 - \epsilon\dfrac{\mathrm{d}^2}{\mathrm{d}y^2} \text{ if } 0 \le y \le 1, \\ n\mathrm{i}\left(k_c U_{0_c} - \omega_c\right) + 2\beta(1+\alpha_c) U_{0_c} + \epsilon(nk_c)^2 - \epsilon\dfrac{\mathrm{d}^2}{\mathrm{d}y^2} \text{ if } -B_v \le y \le 0, \end{cases} \tag{6.9a}$$

$$J_n = nik_c F^{-2} - \beta U_{0_c}^2, \tag{6.9b}$$

$$K_n = \begin{cases} n\mathrm{i}\left(k_c U_{0_c} - \omega_c\right) + \beta U_{0_c} + \epsilon(nk_c)^2 - \epsilon\dfrac{\mathrm{d}^2}{\mathrm{d}y^2} \text{ if } 0 \le y \le 1, \\ n\mathrm{i}\left(k_c U_{0_c} - \omega_c\right) + \beta(1+\alpha_c) U_{0_c} + \epsilon(nk_c)^2 - \epsilon\dfrac{\mathrm{d}^2}{\mathrm{d}y^2} \text{ if } -B_v \le y \le 0, \end{cases} \tag{6.9c}$$

$$L_n = nik_c, \tag{6.9d}$$

$$P_n = -n\mathrm{i}(\omega_c - k_c U_{0_c}), \tag{6.9e}$$

where ω_c is the eigenvalue corresponding to k_c and ϕ_c. Because ω_c is located at the neutral curve, its imaginary part is zero. The boundary and matching conditions of (6.8) are similar

to (4.4)-(4.5):

$$\frac{\mathrm{d}U_{11}}{\mathrm{d}y} = 0 \qquad \text{at} \qquad y = -B_v, 1, \tag{6.10a}$$

$$V_{11} = 0 \qquad \text{at} \qquad y = -B_v, 1, \tag{6.10b}$$

$$\lim_{y\to+0}\left(U_{11}, V_{11}, H_{11}, \frac{\mathrm{d}U_{11}}{\mathrm{d}y}, \frac{\mathrm{d}V_{11}}{\mathrm{d}y}\right) = \lim_{y\to-0}\left(U_{11}, V_{11}, H_{11}, \frac{\mathrm{d}U_{11}}{\mathrm{d}y}, \frac{\mathrm{d}V_{11}}{\mathrm{d}y}\right). \tag{6.10c}$$

Equations (6.8) are solved similarly to the equations in the linear stability analysis, with U_{11}, V_{11} and H_{11} being expanded using the Chebyshev polynomials as in (4.6)-(4.7). The expansions are evaluated at the Gauss-Lobatto points defined by (4.8) and a system of $6(N+1)$ algebraic equations with $6(N+1)$ unknown coefficients. Eight equations are then replaced by four boundary and four matching conditions from (6.10). The resulting algebraic linear system takes the following form:

$$\mathcal{M}_{11}\begin{bmatrix} a_{11_0} \\ a_{11_1} \\ \vdots \\ a_{11_{6N+5}} \end{bmatrix} = 0, \tag{6.11}$$

where $\mathcal{M}_{11}$ is $\mathcal{M}$ with α, k and ω replaced by α_c, k_c and ω_c, respectively, and $a_{11_0}, a_{11_1}, a_{11_2}$, ..., $a_{11_{6N+5}}$ are the unknown coeffients to be obtained from the solution of (6.11).

6.2 $O(\zeta^2)$

Substituting (6.1)-(6.4) and the solutions at $O(\zeta)$ into (2.19), we obtain the following equations at $O(\zeta^2)$:

$$G\hat{U}_2 + \frac{\mathrm{d}U_{0_c}}{\mathrm{d}y}\hat{V}_2 + J\hat{H}_2 = A^2E^2I_{22}^{(1)} + \text{c.c.} + AA^*I_{20}^{(1)}, \tag{6.12a}$$

$$K\hat{V}_2 + F^{-2}\frac{\partial \hat{H}_2}{\partial y} = A^2E^2I_{22}^{(2)} + \text{c.c.} + AA^*I_{20}^{(2)}, \tag{6.12b}$$

$$\frac{\partial \hat{U}_2}{\partial x} + \frac{\partial \hat{V}_2}{\partial y} + P\hat{H}_2 = A^2E^2I_{22}^{(3)} + \text{c.c.} + AA^*I_{20}^{(3)}, \tag{6.12c}$$

where the asterisk denotes complex conjugate and $I_{20}^{(j)}$ and $I_{22}^{(j)}$ $(j = 1, 2, 3)$ are nonlinear terms composed of the solutions at $O(0)$ and $O(\zeta)$ and their derivatives. $I_{20}^{(j)}$ and $I_{22}^{(j)}$ $(j = 1, 2, 3)$ are shown in Appendix B.

At $O(\zeta^2)$, the fundamental perturbations are assumed to have the form:

$$\hat{U}_2(x, y, t) = A^2 U_{22}(y) E^2 + \text{c.c.} + AA^* U_{20}(y) + U_{00}(y), \tag{6.13a}$$

$$\hat{V}_2(x, y, t) = A^2 V_{22}(y) E^2 + \text{c.c.} + AA^* V_{20}(y), \tag{6.13b}$$

$$\hat{H}_2(x, y, t) = A^2 H_{22}(y) E^2 + \text{c.c.} + AA^* H_{20}(y). \tag{6.13c}$$

The base flow velocity at $y = -B_v$ is ϕ_c when considering the neutral state. However, the actual velocity at $y = -B_v$ is $\phi_c - \zeta^2$. A corrective term $U_{00}(y)$ is then introduced in (6.13a) because ϕ is perturbed as $\phi_c - \zeta^2$. The base state velocity U_0 is expanded as

$$U_0 = U_{0_c} + \zeta^2 U_{00}, \tag{6.14}$$

where U_{0_c} is U_0 corresponding to ϕ_c. Substituting (6.1) and (6.14) into (3.1), we have the following equations at $O(\zeta^2)$:

$$2\beta U_{0_c} U_{00} - \epsilon \frac{\mathrm{d}^2 U_{00}}{\mathrm{d}y^2} = 0 \qquad \text{if} \qquad 0 \le y \le 1, \tag{6.15a}$$

$$2\beta\,(1+\alpha_c)\; U_{0_c} U_{00} - \epsilon \frac{\mathrm{d}^2 U_{00}}{\mathrm{d}y^2} = -2\beta\,(1+\alpha_c)^{1/2} - 2\epsilon\,(1+\alpha_c)\,\frac{\mathrm{d}U_{0_c}}{\mathrm{d}y} \qquad \text{if} \qquad -B_v \le y \le 0. \tag{6.15b}$$

The above equations are supplemented by the following boundary and matching conditions:

$$\frac{\mathrm{d}U_{00}}{\mathrm{d}y} = 0 \quad \text{at} \quad \tilde{y} = 1, -B_v, \tag{6.16a}$$

$$\lim_{y \to +0} \left(U_{00}, \frac{\mathrm{d}U_{00}}{\mathrm{d}y} \right) = \lim_{y \to -0} \left(U_{00}, \frac{\mathrm{d}U_{00}}{\mathrm{d}y} \right). \tag{6.16b}$$

In order to solve (6.15) under the boundary and matching conditions (6.16), we expand

U_{00} using the Chebyshev polynomials as in (4.6) and (4.7). As in (4.6) and (4.7), different expansions of U_{00} are employed in the non-vegetated and vegetated zones. From evaluating the expanded equations and boundary and matching conditions at the Gauss-Lobatto points defined as in (4.8), we obtain an algebraic system which takes the form

$$\mathcal{M}_{00}\begin{bmatrix} a_{00_0} \\ a_{00_1} \\ \vdots \\ a_{00_{2N+1}} \end{bmatrix} = \begin{bmatrix} f_{00_0}(y) \\ f_{00_1}(y) \\ \vdots \\ f_{00_{2N+1}}(y) \end{bmatrix}, \tag{6.17}$$

where $\mathcal{M}_{00}$ is the $2\,(N+1)\times 2\,(N+1)$ matrix of the unknown coefficients $a_{00_0}, a_{00_1}, a_{00_2}$, ..., $a_{00_{6N+5}}$, and $f_{00_i}(y)$ $(i = 1, ..., 2N+1)$ corresponds to the terms of (6.15) and (6.16) which do not contain U_{00}.

Substituting (6.13) into (6.12), we have the following equations composed of terms with A^2E^2:

$$G_2U_{22} + \frac{\mathrm{d}U_{0_c}}{\mathrm{d}y}V_{22} + J_2H_{22} = I_{22}^{(1)}, \tag{6.18a}$$

$$K_2V_{22} + F^{-2}\frac{\mathrm{d}H_{22}}{\mathrm{d}y} = I_{22}^{(2)}, \tag{6.18b}$$

$$L_2U_{22} + \frac{\mathrm{d}V_{22}}{\mathrm{d}y} + P_2H_{22} = I_{22}^{(3)}, \tag{6.18c}$$

and the following equations composed of terms with AA^*:

$$G_0U_{20} + \frac{\mathrm{d}U_{0_c}}{\mathrm{d}y}V_{20} + J_2H_{20} = I_{20}^{(1)}, \tag{6.19a}$$

$$K_0V_{20} + F^{-2}\frac{\mathrm{d}H_{20}}{\mathrm{d}y} = I_{20}^{(2)}, \tag{6.19b}$$

$$\frac{\mathrm{d}V_{20}}{\mathrm{d}y} = I_{20}^{(3)}. \tag{6.19c}$$

Equations (6.18) and (6.19) are supplemented by boundary and matching conditions similar

to (4.4)-(4.5), as follows:

$$\frac{\mathrm{d}U_{22}}{\mathrm{d}y} = 0 \qquad \text{at} \qquad y = -B_v, 1, \tag{6.20a}$$

$$V_{22} = 0 \qquad \text{at} \qquad y = -B_v, 1, \tag{6.20b}$$

$$\lim_{y\to+0}\left(U_{22}, V_{22}, H_{22}, \frac{\mathrm{d}U_{22}}{\mathrm{d}y}, \frac{\mathrm{d}V_{22}}{\mathrm{d}y}\right) = \lim_{y\to-0}\left(U_{22}, V_{22}, H_{22}, \frac{\mathrm{d}U_{22}}{\mathrm{d}y}, \frac{\mathrm{d}V_{22}}{\mathrm{d}y}\right), \tag{6.20c}$$

$$\frac{\mathrm{d}U_{20}}{\mathrm{d}y} = 0 \qquad \text{at} \qquad y = -B_v, 1, \tag{6.21a}$$

$$V_{20} = 0 \qquad \text{at} \qquad y = -B_v, 1, \tag{6.21b}$$

$$\lim_{y\to+0}\left(U_{20}, V_{20}, H_{20}, \frac{\mathrm{d}U_{20}}{\mathrm{d}y}, \frac{\mathrm{d}V_{20}}{\mathrm{d}y}\right) = \lim_{y\to-0}\left(U_{20}, V_{20}, H_{20}, \frac{\mathrm{d}U_{20}}{\mathrm{d}y}, \frac{\mathrm{d}V_{20}}{\mathrm{d}y}\right), \tag{6.21c}$$

The procedure for solving the system of equations (6.18) is similar to the one employed for solving (6.9). The resulting algebraic linear system takes the form:

$$\mathcal{M}_{22}\begin{bmatrix} a_{22_0} \\ a_{22_1} \\ \vdots \\ a_{22_{6N+5}} \end{bmatrix} = \begin{bmatrix} f_{22_0}(y) \\ f_{22_1}(y) \\ \vdots \\ f_{22_{6N+5}}(y) \end{bmatrix}, \tag{6.22}$$

where $\mathcal{M}_{22}$ is the matrix in which the elements consist of the coefficients of the unknown terms $a_{22_0}, a_{22_1}, a_{22_2}, ..., a_{22_{6N+5}}$. The terms $f_{22_i}(y)$ $(i = 1, ..., 6N + 5)$ correspond to $I_{22}^{(j)}$ $(j = 1, 2, 3)$, with the exception of eight terms which take the value of zero in correspondence with the boundary and matching conditions (6.20).

Equation (6.19c) can be solved analytically using two out of the four boundary and matching conditions (6.21) which contain the term V_{20} or its derivative. Although only the first derivative appears in the left-hand side of (6.19c), two conditions are necessary to solve (6.19c) because $I_{20}^{(3)}$ is different in the non-vegetated and vegetated zones. $I_{20}^{(3)}$ is a function of V_{11} and H_{11} (see (B.3)), which are different in each zone.

Following the determination of V_{20} from the analytical solution of (6.19c), H_{20} is then determined from the analytical solution of (6.19b). Because only one condition in (6.20)

contains H_{20} while two conditions are necessary to solve (6.19b) in the non-vegetated and vegetated zones, an undetermined integration constant is added to the solution of H_{20}.

In order to solve (6.19a), U_{20} is expanded using the Chebyshev polynomials similarly to (4.6) and (4.7). From evaluating the expanded equations and boundary and matching conditions at the Gauss-Lobatto points defined as in (4.8), we obtain the following algebraic system:

$$\mathcal{M}_{00}\begin{bmatrix} a_{20_0} \\ a_{20_1} \\ \vdots \\ a_{20_{2N+1}} \end{bmatrix} = \begin{bmatrix} f_{20_0}(y) \\ f_{20_1}(y) \\ \vdots \\ f_{20_{2N+1}}(y) \end{bmatrix}, \tag{6.23}$$

where $f_{20_i}(y)$ $(i = 1, ..., 2N + 1)$ corresponds to the terms of (6.19a) which do not contain U_{20}, and to the terms which assume the value of zero which are obtained from the boundary and matching conditions.

In order to determine the integration constant introduced to the solution of H_{20}, we introduce a condition of conservation of flow discharge (Q) in the form:

$$Q = \frac{1}{T}\int_0^T \int_{-Bv}^1 UH \mathrm{d}y\mathrm{d}t, \tag{6.24}$$

where T is a period of time long enough so that the average of the fluctuating terms vanishes. A sufficiently long distance in the streamwise direction could also have been employed instead. Introducing the expansions up to the order of $O(\zeta^2)$ into the above, we have:

$$Q = \int_{-Bv}^1 \left\{U_{0_c}(y) + \zeta^2 \left[U_{00}(y) + AA^* \left(H_{20}(y)U_0(y) + U_{20}(y) + U_{11}(y)H_{11}^*(y) + \text{c.c.}\right)\right]\right\}\mathrm{d}y, \tag{6.25}$$

where the terms containing E vanish in the long time average. Because the flow discharge is conserved in the base state, the following relation holds:

$$\int_{-Bv}^1 \left[H_{20}(y)U_0(y) + U_{20}(y) + U_{11}(y)H_{11}^*(y) + \text{c.c.}\right]\mathrm{d}y = 0, \tag{6.26}$$

The unknown constant introduced to H_{20} is determined from the solution of the above

equation.

The variables with the subscript 20 reflect the changes in the time-averaged flow velocities and flow depth due to a change in the velocity distribution.

6.3 $O(\zeta^3)$

Substituting (6.1)-(6.4) and the solutions at $O(0)$, $O(\zeta)$ and $O(\zeta^2)$ into (2.19), we obtain the following equations at $O(\zeta^3)$:

$$G\hat{U}_3 + \frac{\mathrm{d}U_0}{\mathrm{d}y}\hat{V}_3 + J\hat{H}_3 = A^3E^3I_{33}^{(1)} + \text{c.c.} + \left[A^2A^*I_{31}^{(1)} + AI_{31}^{(2)} + \frac{\mathrm{d}A}{\mathrm{d}t_1}I_{31}^{(3)}\right]E + \text{c.c.}, \tag{6.27a}$$

$$K\hat{V}_3 + F^{-2}\frac{\partial \hat{H}_3}{\partial y} = A^3E^3I_{33}^{(2)} + \text{c.c.} + \left[A^2A^*I_{31}^{(4)} + AI_{31}^{(5)} + \frac{\mathrm{d}A}{\mathrm{d}t_1}I_{31}^{(6)}\right]E + \text{c.c.}, \tag{6.27b}$$

$$\frac{\partial \hat{U}_3}{\partial x} + \frac{\partial \hat{V}_3}{\partial y} + P\hat{H}_3 = A^3E^3I_{33}^{(3)} + \text{c.c.} + \left[A^2A^*I_{31}^{(7)} + AI_{31}^{(8)} + \frac{\mathrm{d}A}{\mathrm{d}t_1}I_{31}^{(9)}\right]E + \text{c.c.}, \tag{6.27c}$$

where $I_{31}^{(i)}$ $(i = 1, ..., 9)$ and $I_{33}^{(j)}$ $(j = 1, 2, 3)$ are nonlinear terms composed of the solutions at $O(\zeta)$ and $O(\zeta^2)$ and their derivatives.

At $O(\zeta^3)$, the fundamental perturbations are assumed to have the form:

$$\hat{U}_3(x, y, t) = A^3U_{33}(y)E^3 + \text{c.c.} + U_{31}(y, t_1)E + \text{c.c.}, \tag{6.28a}$$

$$\hat{V}_3(x, y, t) = A^3V_{33}(y)E^3 + \text{c.c.} + V_{31}(y, t_1)E + \text{c.c.}, \tag{6.28b}$$

$$\hat{H}_3(x, y, t) = A^3H_{33}(y)E^3 + \text{c.c.} + H_{31}(y, t_1)E + \text{c.c.}. \tag{6.28c}$$

Substituting the above expansions into (6.27), we have the following equations composed

of terms with E (excluding E^3):

$$G_1 U_{31} + \frac{\mathrm{d}U_0}{\mathrm{d}y} V_{31} + J_1 H_{31} = \left[A^2 A^* I_{31}^{(1)} + A I_{31}^{(2)} + \frac{\mathrm{d}A}{\mathrm{d}t_1} I_{31}^{(3)} \right], \tag{6.29a}$$

$$K_1 V_{31} + F^{-2} \frac{\mathrm{d}H_{31}}{\mathrm{d}y} = \left[A^2 A^* I_{31}^{(4)} + A I_{31}^{(5)} + \frac{\mathrm{d}A}{\mathrm{d}t_1} I_{31}^{(6)} \right], \tag{6.29b}$$

$$L_1 U_{31} + \frac{\mathrm{d}V_{31}}{\mathrm{d}y} + P_1 H_{31} = \left[A^2 A^* I_{31}^{(7)} + A I_{31}^{(8)} + \frac{\mathrm{d}A}{\mathrm{d}t_1} I_{31}^{(9)} \right]. \tag{6.29c}$$

The boundary and matching conditions of the above equations are similar to (4.4)-(4.5):

$$\frac{\mathrm{d}U_{31}}{\mathrm{d}y} = 0 \qquad \text{at} \qquad y = -B_v, 1, \tag{6.30a}$$

$$V_{31} = 0 \qquad \text{at} \qquad y = -B_v, 1, \tag{6.30b}$$

$$\lim_{y \to +0} \left(U_{31}, V_{31}, H_{31}, \frac{\mathrm{d}U_{31}}{\mathrm{d}y}, \frac{\mathrm{d}V_{31}}{\mathrm{d}y} \right) = \lim_{y \to -0} \left(U_{31}, V_{31}, H_{31}, \frac{\mathrm{d}U_{31}}{\mathrm{d}y}, \frac{\mathrm{d}V_{31}}{\mathrm{d}y} \right). \tag{6.30c}$$

From expanding U_{31}, V_{31} and H_{31} using the Chebyshev polynomials as in (4.7) and evaluating the resulting equations at the Gauss-Lobatto points as in (4.8), we have a linear system obtained from (6.29) with eight equations replaced by conditions expressed in (6.30) which takes the form:

$$\mathcal{M}_{11} \begin{bmatrix} a_{31_0}(t_1) \\ a_{31_1}(t_1) \\ \vdots \\ a_{31_{6N+5}}(t_1) \end{bmatrix} = \begin{bmatrix} f_{31_0}(y, t_1) \\ f_{31_1}(y, t_1) \\ \vdots \\ f_{31_{6N+5}}(y, t_1) \end{bmatrix}, \tag{6.31}$$

where f_{31_i} $(i = 1, ..., 6N + 5)$ are nonhomogeneous solutions obtained from the right-hand side terms of (6.29), with the exception of eight terms which take the value of zero in correspondence with the boundary and matching conditions (6.30).

Because the non-homogeneous part of (6.31) admits a non-trivial solution, a solvability condition has to be satisfied. This condition is that the determinant of $\mathcal{M}_{11}$ with one of its columns replaced by the right-hand side column vector should vanish. This linear algebraic

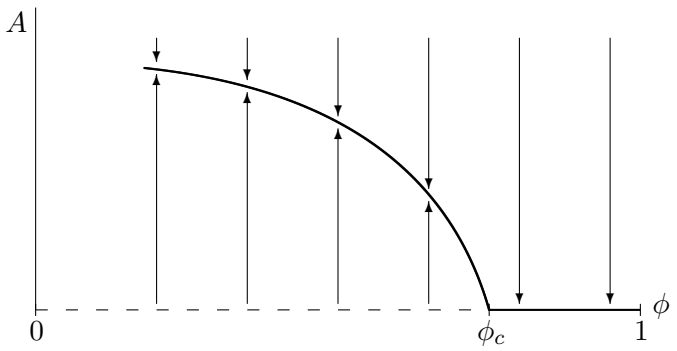

Figure 6-1: Supercritical bifurcation based on the expansion of the ratio between the undisturbed velocities ϕ.

system reduces to the following Landau equation:

$$\frac{dA}{dt_1} = \eta_0 A + \eta_1 |A|^2 A, \tag{6.32}$$

where η_0 is the linear growth rate of the amplitude and η_1 is the first Landau constant.

The signs of the real parts of η_0 and η_1 determine the bifurcation pattern. In the case of $\mathrm{Re}(\eta_0) > 0$ and $\mathrm{Re}(\eta_1) < 0$, we have supercritical bifurcation, where a steady state with an equilibrium amplitude A_e is reached as $t_1 \to \infty$. From (6.32), we have

$$|A_e| = \sqrt{-\frac{\mathrm{Re}(\eta_0)}{\mathrm{Re}(\eta_1)}}. \tag{6.33}$$

The phase μ of the amplitude is also derived from (6.32),

$$A_e = |A_e|\, e^{i\mu t_1}, \tag{6.34a}$$

$$\mu = \mathrm{Im}(\eta_0) + \mathrm{Im}(\eta_1)\, |A_e|^2 . \tag{6.34b}$$

Fig. 6-1 illustrates the equilibrium amplitude in the case of supercritical bifurcation based on the expansion of the ratio between the undisturbed velocity in the vegetated zone and the undisturbed velocity in the vegetated zone, ϕ.

Fig. 6-2 presents a comparison between the base state velocity U_0 and the time-averaged normalized velocity $\overline{U}$, referent to run 3 (as in Table 7.3) of the experiments described in Ikeda et al. (1991). The gradient of $\overline{U}$ is milder due to the increase of the mixing layer around the boundary between the non-vegetated and vegetated zones. Fig. 6-3 presents

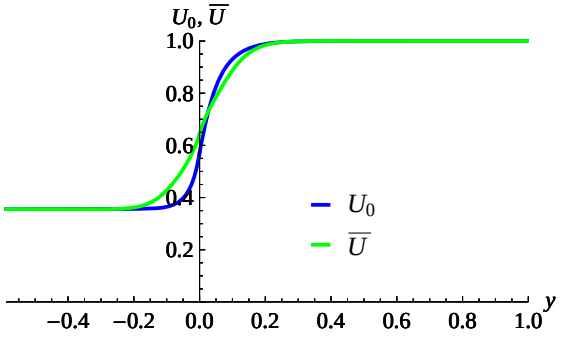

Figure 6-2: Base state and time averaged velocity profiles (run 3 of Ikeda et al. (1991)).

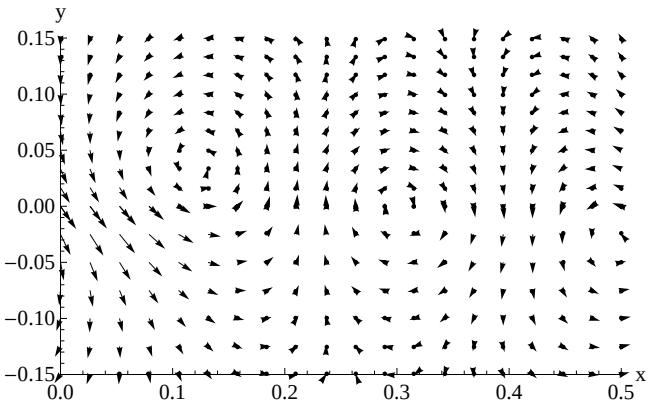

Figure 6-3: Fluctuating normalized velocity vectors (run 3 of Ikeda et al. (1991)).

normalized fluctuating velocity (i.e., $\sqrt{U^2 + V^2} - \overline{U}$) vectors up to the order of $O(\zeta^2)$, also referent to run 3.

Chapter 7

Results and discussion: nonlinear stability analysis

7.1 Supercritical bifurcation

The neutral curve in the $\phi - k$ plane can depicted once the parameters β, ϵ, B_v and F are specified. Hereafter, ϕ_c will be taken as the maximum value of ϕ which lays on the neutral curve in $\phi - k$ plane. A sample neutral curve in the $\phi - k$ plane is depicted in Fig 7-1.

In this section, we derive the Landau equation for multiple values of β and ϵ, while the parameters F and B_v are kept constant ($F = 0.5$ and $B_v = 0.55$). As seen in Fig. 5-6, the minimum α_c, which corresponds to the maximum ϕ_c, does not vary when F increases from 0.5 to 1.5. And because of the gravitational instability, a minimum threshold α_c dividing the plane into a stable and an unstable region cannot be defined for $F = 2.5$. Therefore, the variation of F is not considered herein. And because the neutral instability does not vary significantly due to B_v, except when B_v is sufficiently small, as depicted in Fig. 5-4, this parameter is also kept constant herein.

The parameter ϕ_c, its corresponding k_c in the neutral curve in the $\phi - k$ plane, and the determined linear growth rate η_0 and the first Landau constant η_1 are presented in Table 7.1, for multiple values of β, and Table 7.2, for multiple values of ϵ.

Supercritical bifurcation is found to occur for values of β within the range of $0.032 - 0.316$ in Table 7.1, as $\mathrm{Re}(\eta_0)$ is positive and $\mathrm{Re}(\eta_1)$ is negative in this range. However,

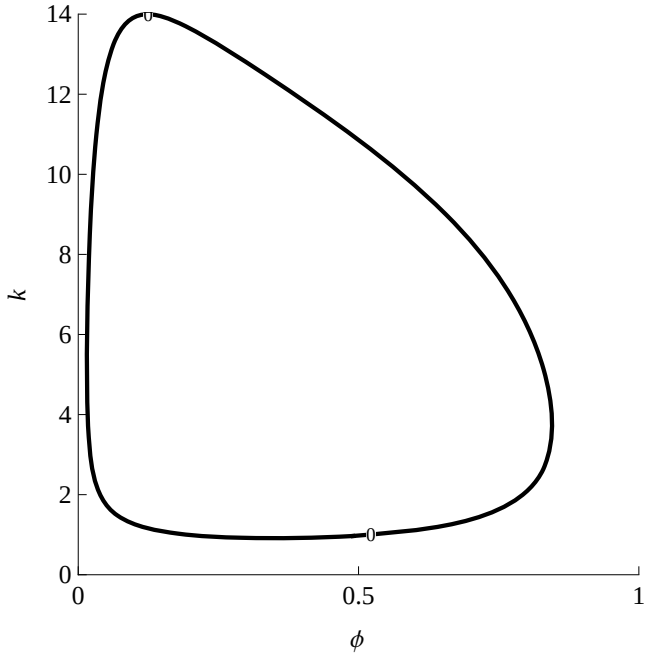

Figure 7-1: Neutral curve in the $\phi - k$ plane for the case $\beta = 0.05$, $\epsilon = 6 \times 10^{-4}$, $B_v = 0.55$, $F = 0.5$.

Table 7.1: Parameters on the neutral curve in the $\phi - k$ plane for the case $\epsilon = 6 \times 10^{-4}$, $B_v = 0.55$, $F = 0.5$ and multiple values of β; and the real and imaginary parts of η_0 and η_1.

β	C_f	A_R	ϕ_c	k_c	$\mathrm{Re}(\eta_0)$	$\mathrm{Im}(\eta_0)$	$\mathrm{Re}(\eta_1)$	$\mathrm{Im}(\eta_1)$
0.010	0.0020	5.0	0.903	2.07	-3.64	-0.36	581	149
0.018	0.0029	6.0	0.892	2.53	-1.00	-1.08	-54	-28
0.032	0.0043	7.3	0.871	3.14	2.13	-1.23	-163	-92
0.056	0.0064	8.9	0.837	3.94	0.83	-3.16	-192	-10
0.100	0.0093	10.7	0.784	5.07	1.03	-3.25	-206	-24
0.178	0.0137	13.0	0.706	6.71	1.30	-3.02	-226	-44
0.316	0.0201	15.7	0.584	9.19	1.56	-1.72	-246	-75
0.562	0.0295	19.1	Stable					

Table 7.2: Parameters on the neutral curve in the $\phi - k$ plane for the case $\beta = 0.05$, $B_v = 0.55$, $F = 0.5$ and multiple values of ϵ; and the real and imaginary parts of η_0 and η_1.

ϵ	C_f	A_R	ϕ_c	k_c	$\mathrm{Re}(\eta_0)$	$\mathrm{Im}(\eta_0)$	$\mathrm{Re}(\eta_1)$	$\mathrm{Im}(\eta_1)$
1.78×10^{-5}	0.0006	88.9	0.974	19.33	4.34	-173.42	-12005	-198
3.16×10^{-5}	0.0008	60.6	0.967	14.29	3.20	-107.92	-6184	-115
5.62×10^{-5}	0.0012	41.3	0.956	10.73	2.40	-61.62	-3060	-79
1.00×10^{-4}	0.0018	28.1	0.941	8.11	1.80	-33.79	-1515	-52
1.78×10^{-4}	0.0026	19.2	0.921	6.19	1.35	-17.55	-759	-33
3.16×10^{-4}	0.0038	13.0	0.893	4.82	1.02	-7.99	-386	-17
5.62×10^{-4}	0.0056	8.9	0.851	3.85	0.78	-3.67	-210	-10
1.00×10^{-3}	0.0083	6.1	0.784	3.14	0.64	0.71	-36	27
1.78×10^{-3}	0.0121	4.1	0.667	2.62	0.10	-0.23	-117	-28
3.16×10^{-3}	0.0178	2.8	0.405	2.33	-0.72	-0.60	64	56
5.62×10^{-3}	0.0261	1.9	Stable					

because $\mathrm{Re}(\eta_0)$ for $\beta = 0.032$ is larger than $\mathrm{Re}(\eta_0)$ for larger values of β when it was expected to be smaller, we can assume that this result is not reliable. Moreover, negative $\mathrm{Re}(\eta_0)$ were obtained for $\beta = 0.10$ and $\beta = 0.18$, while all values of $\mathrm{Re}(\eta_0)$ should be positive because the instability occurs when $\phi < \phi_c$. Therefore, the results in the range of $\beta \lessapprox 0.032$ are not reliable. This is attributed to the fact that the channel is not wide enough to accommodate the shear layer, which further increases once nonlinear terms are considered, as depicted in Fig 6-2. The flow is stable for any ϕ in the range of $\beta \gtrapprox 0.562$.

In Table 7.2, the values of η_0 and η_1 are not correct in the range of $\epsilon \gtrapprox 1.00 \times 10^{-3}$, also because of the small aspect ratio of the channel. In the range of $\epsilon \gtrapprox 5.62 \times 10^{-3}$, however, the flow is expected to be stable, which is in agreement with Fig. 5-2. Supercritical bifurcation is found to occur for all values of $\epsilon \lessapprox 5.62 \times 10^{-4}$.

7.1.1 Critical vegetation drag and density

The neutral curves in the $\phi - k$ plane for various β or ϵ typically posses a maximum ϕ_c, above which the flow is stable. Therefore, there is typically a minimum critical vegetation drag and density parameter α_c below which the flow is stable. Fig. 7-2 (a) and (b) depict the minimum α_c as functions of β and ϵ, respectively.

The flow is less stable in the range of small and large β, for which correspond larger values of α_c. α_c is minimized when β is around 0.08. As previously mentioned, the role of β on the instabilities due to the transverse mixing is dual, as the increase of β can both enhance or damp these instabilities. For a large β, the bed shear stress effects overlaps the effect of lateral mixing, while in the range of small β, the velocity gradient which enhances the lateral mixing is milder. Although the shallow water approach is not valid in the range of small β, an increasing of α_c is expect to take place at this range.

The increase of ϵ makes the flow less unstable because the effect of the sub-depth-scale eddy viscosity suppresses the effect of transverse mixing. Therefore, for a larger ϵ, a larger α_c is necessary for the flow to become unstable, as observed in Fig. 7-2 (b).

7.1.2 Equilibrium amplitude

The absolute value of the equilibrium amplitude ($|A_e|$) was determined from (6.33) for the ranges of β and ϵ which correspond to supercritical bifurcation. Fig 7-3 (a) and (b) depict $|A_e|$ as functions of β and ϵ respectively.

In Fig 7-3(a), $|A_e|$ increases, tends to stabilize and then slightly decreases with the increase of β. While we have found that the flow is less unstable in the range of sufficiently large or small β, herein we also have to consider that the transverse mixing may be enhanced by the smaller ϕ_c in the range of large β. Similarly, in Fig 7-3(b), while the flow is expected to be less unstable in the range of large ϵ, the corresponding ϕ_c is this region will be small, which may enhance the instabilities and result in higher amplitudes.

7.1.3 Maximum friction velocity

We can define a friction velocity (U_{fM}) by the lateral shear stress due to the transverse mixing as

$$U_{fM}^2 = -\overline{U'V'}, \tag{7.1}$$

where U' and V' are the fluctuations of the streamwise and transverse velocities, respectively.

Fig. 7-4 presents a sample curve of $-\overline{U'V'}$ as a function of y for the case $\beta = 0.05$,

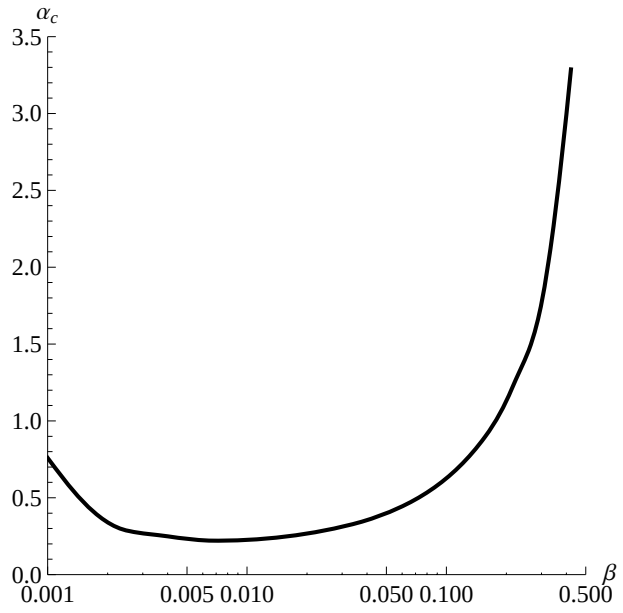

(a)

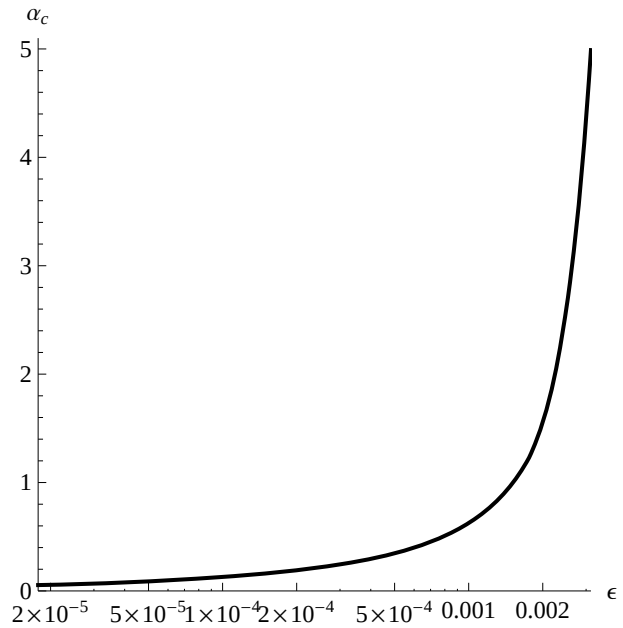

(b)

Figure 7-2: α_c as functions of (a) β for the case $\epsilon = 6 \times 10^{-4}$, (b) ϵ for the case $\beta = 0.05$; in both cases $B_v = 0.55$, $F = 0.5$.

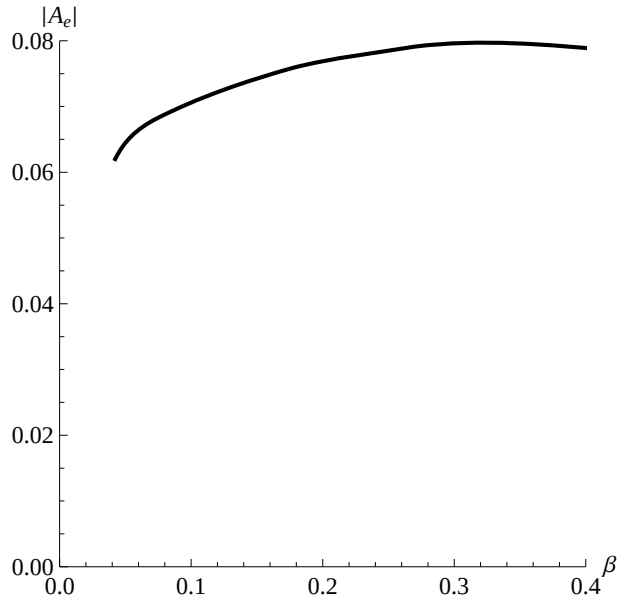

(a)

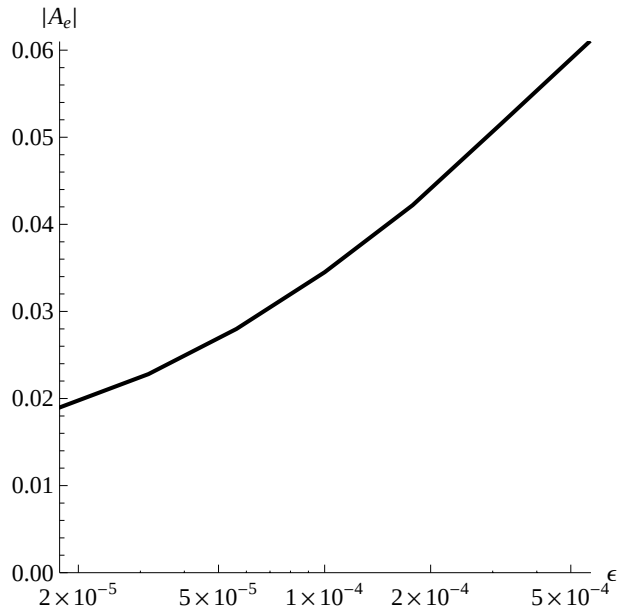

(b)

Figure 7-3: Absolute value of the equilibrium amplitude ($|A_e|$) as functions of (a) β for the case $\epsilon = 6 \times 10^{-4}$, (b) ϵ for the case $\beta = 0.05$; in both cases $B_v = 0.55$, $F = 0.5$.

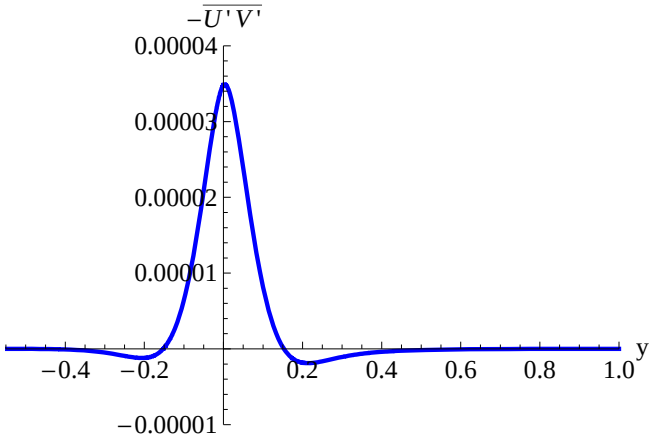

Figure 7-4: $-\overline{U'V'}$ as a function of y for the case $\beta = 0.05$, $\epsilon = 6 \times 10^{-4}$, $B_v = 0.55$, $F = 0.5$, $\zeta^2 = 0.01$.

$\epsilon = 6 \times 10^{-4}$, $B_v = 0.55$, $F = 0.5$, and $\zeta^2 = 0.01$. As depicted in this figure, $-\overline{U'V'}$ reaches its maximum at $y = 0$. Therefore the friction velocity U_{fM} reaches its maximum at the boundary between the non-vegetated and the vegetated zone. Far from this boundary, $-\overline{U'V'}$ decays to zero.

Fig 7-5 (a) and (b) depicts the maximum friction velocity as functions of β and ϵ, respectively. The behavior of $U_{fM,max}$ is found to be similar to the behavior of the amplitude as functions of β or ϵ in Fig 7-5. The value of $U_{fM,max}$ is obviously expect to increase with $|A_e|$, since the fluctuating terms increase with $|A_e|$. Because a small ζ is employed in Fig 7-5, which will lead to very small higher order terms of ζ, there is a quasi-linear correlation between the amplitude in Fig 7-3 and $U_{fM,max}$ in Fig 7-5.

7.1.4 Lateral large-scale kinematic eddy viscosity

In the fully developed stage of perturbations, the Reynolds stress can be determined from the fluctuating velocities U' and V'. Using Boussinesq's kinematic eddy viscosity, the following relation holds:

$$-\rho\overline{U'V'} = \rho\epsilon_M \frac{\mathrm{d}\overline{U}}{\mathrm{d}y}, \tag{7.2}$$

where ϵ_M is the lateral kinematic eddy viscosity at the fully developed stage of perturbations. ϵ_M is normalized by the undisturbed velocity in the non-vegetated zone, $\tilde{U}_\infty$, and the

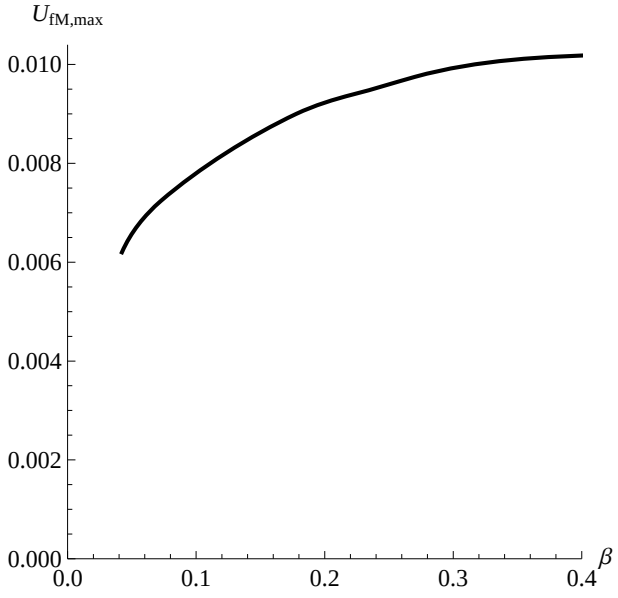

(a)

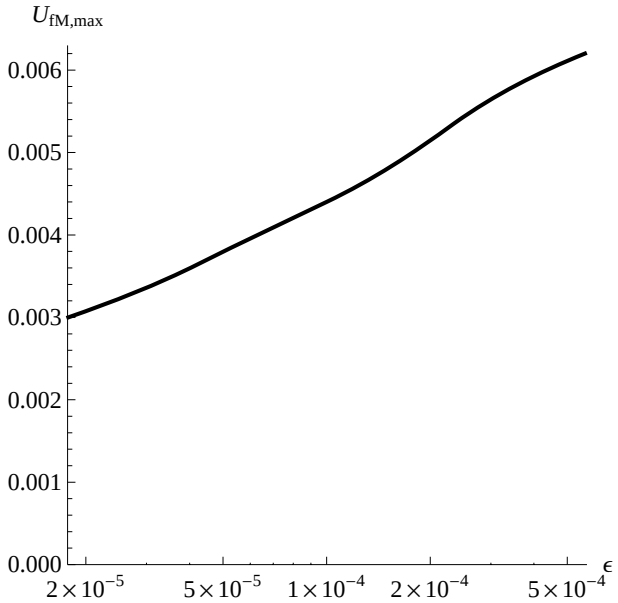

(b)

Figure 7-5: $U_{fm,max}$ as a function of (a) β for the case $\epsilon = 6 \times 10^{-4}$, (b) ϵ for the case $\beta = 0.05$; in both cases $B_v = 0.55$, $F = 0.5$, $\zeta^2 = 0.01$.

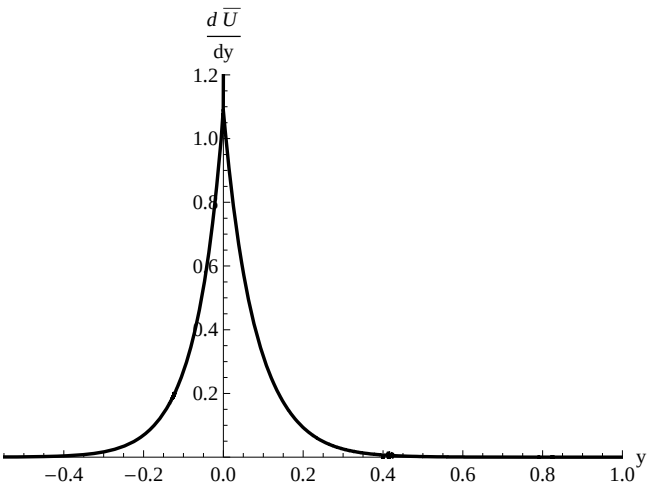

Figure 7-6: $\mathrm{d}\overline{U}/\mathrm{d}y$ as a function of y for the case $\beta = 0.05$, $\epsilon = 6 \times 10^{-4}$, $B_v = 0.55$, $F = 0.5$, $\zeta^2 = 0.01$.

width of the non-vegetated zone, $\tilde{B}$, as in (2.21).

Fig. 7-6 presents a sample curve of $\mathrm{d}\overline{U}/\mathrm{d}y$ as a function of y for the case $\beta = 0.05$, $\epsilon = 6 \times 10^{-4}$, $B_v = 0.55$, $F = 0.5$, and $\zeta^2 = 0.01$. Similarly to $-\overline{U'V'}$ in Fig. 7-4, $\mathrm{d}\overline{U}/\mathrm{d}y$ has a maximum at $y = 0$ and decays to zero far from the interface between the non-vegetated and vegetated zones. And differently from $-\overline{U'V'}$, $\mathrm{d}\overline{U}/\mathrm{d}y$ has a cusp at $y = 0$.

The kinematic eddy viscosity ϵ_M determined from (7.2) and using the values of β, ϵ, B_v, F and ζ^2 of Fig. 7-4 and Fig. 7-6 is depicted in Fig. 7-7 as a function of y. Because ϵ_M can only be determined in the shear layer, the range of the transverse coordinate y presented in Fig. 7-7 is limited to $-0.15 \leq y \leq 0.15$. ϵ_M has two local points of maximum, one in the non-vegetated zone, and one in the vegetated zone, and a cusp at $y = 0$.

Although ϵ_M is the eddy viscosity which takes into account the effect of the lateral transverse mixing, the values of ϵ_M in Fig. 7-7 are not larger than the value of $\epsilon = 6 \times 10^{-4}$, which is the sub-depth eddy viscosity in the case depicted in Fig. 7-7. This is because a small value of ζ was employed in Fig. 7-7, such that the condition depicted in this figure is not much deviated from the neutral stability. Comparisons between ϵ and ϵ_M for larger values of ζ will be presented in the next section.

Fig 7-8 (a) and (b) depicts the maximum ϵ_M, which can be located either in the non-

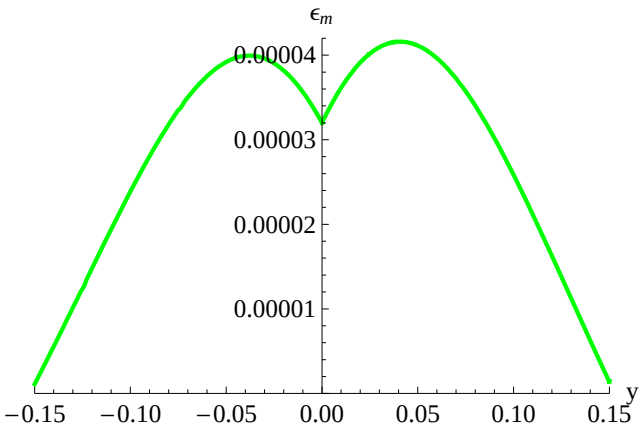

Figure 7-7: Lateral kinematic eddy viscosity in the fully developed stage of perturbations ϵ_M as a function of y for the case $\beta = 0.05$, $\epsilon = 6 \times 10^{-4}$, $B_v = 0.55$, $F = 0.5$, $\zeta^2 = 0.01$.

vegetated or the vegetated zones, as functions of β and ϵ, respectively. While $U'V'$ increases with the increasing of β or ϵ, the velocity gradient $\mathrm{d}\overline{U}/\mathrm{d}y$ at the shear layer becomes steeper with the increase of β and becomes milder with the increase of ϵ, as in Fig. 3-1. Therefore, the effects of increasing β and ϵ on ϵ_M are opposite.

7.2 Comparison with experimental data

The predictive nonlinear analysis developed herein was compared with the results of the laboratory experiments of Ikeda et al. (1991) and White and Nepf (2007). In their experiments, vortices were generated in a channel featuring a lateral array of pile dikes. The major hydraulic variables of their experimental runs are presented in Table 7.3. We predicted supercritical bifurcation for most cases, with the exception of runs II, III and XI, although in the experiments an equilibrium amplitude was also observed in these runs. Runs II, III and XI have in common the small value of β, which is a less favorable condition for predicting supercritical bifurcation, as previously mentioned.

7.2.1 Time-averaged velocity

A comparison between the time-averaged velocity profile along the transverse direction $\tilde{y}$ theoretically determined herein and measurements of Ikeda et al. (1994) is presented in

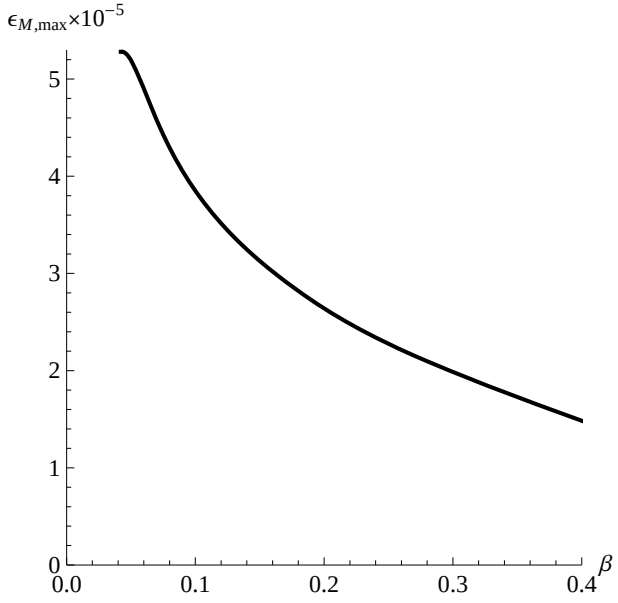

(a)

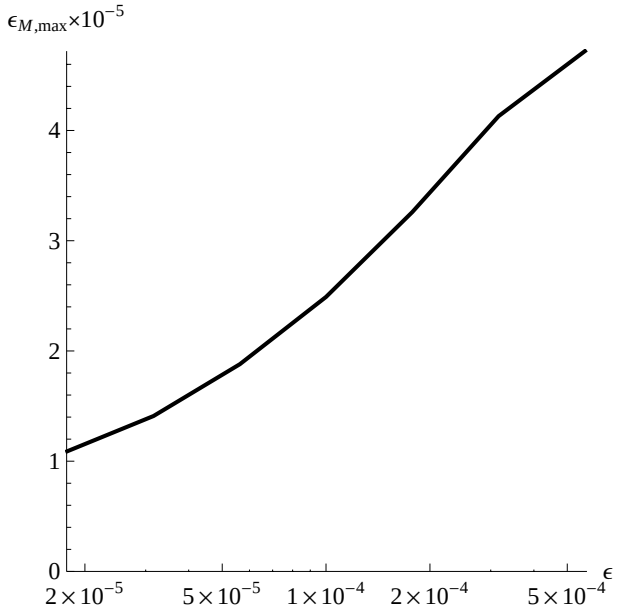

(b)

Figure 7-8: $\epsilon_{m,max}$ as a function of (a) β for the case $\epsilon = 6 \times 10^{-4}$, (b) ϵ for the case $\beta = 0.05$; in both cases $B_v = 0.55$, $F = 0.5$, $\zeta^2 = 0.01$.

Table 7.3: Hydraulic parameters from the experiments of Ikeda et al. (1991) (runs 1–5) and White and Nepf (2007) (runs I–XI).

Run	β	$\epsilon(\times 10^{-4})$	F	ϕ	ϕ_c	k_c	$\mathrm{Re}(\eta_0)$	$\mathrm{Im}(\eta_0)$	$\mathrm{Re}(\eta_1)$	$\mathrm{Im}(\eta_1)$
1	0.061	5.19	0.51	0.303	0.846	4.27	0.88	-1.83	-228	-14.2
2	0.061	5.19	0.77	0.303	0.845	4.27	0.87	-1.63	-228	-14.5
3	0.079	4.48	0.74	0.356	0.838	5.07	1.06	-2.28	-282	-24.5
4	0.164	3.00	0.62	0.462	0.810	8.71	1.82	-4.64	-532	-64.3
5	0.038	6.88	0.48	0.243	0.852	3.16	0.54	-0.99	-154	4.3
I	0.058	3.99	0.22	0.124	0.869	4.71	0.98	-2.12	-300	-11.4
II	0.023	4.73	0.21	0.078	0.900	3.05	-10.82	4.69	538	621.4
III	0.023	7.31	0.21	0.079	0.861	2.65	0.39	-0.77	61	20.1
IV	0.064	4.02	0.22	0.075	0.862	4.94	1.03	-1.98	-303	-15.1
V	0.061	2.82	0.05	0.079	0.890	5.57	1.19	-3.05	-453	-21.7
VI	0.043	2.86	0.16	0.065	0.905	4.78	1.01	-2.58	-421	-8.6
VII	0.055	3.73	0.21	0.024	0.877	4.76	0.99	-1.24	-322	-11.2
VIII	0.126	4.29	0.08	0.034	0.799	6.54	1.36	-0.73	-316	-36.4
IX	0.089	4.95	0.11	0.033	0.818	5.25	1.08	-0.73	-251	-20.8
X	0.066	5.22	0.34	0.030	0.837	4.50	0.92	-0.65	-227	-10.8
XI	0.032	8.70	0.19	0.018	0.827	2.83	0.17	0.13	131	365.6

Fig. 7-12.

The present model reproduces well the velocity gradient around the shear layer. However, the observed gradient may be slightly shifted towards the non-vegetated region, as in (a) and (c). This is because in the mathematical model employed herein, the drag force due to vegetation is assumed as zero at the immediate vicinity of the edge of the vegetated region, as in (2.2), while a non-zero vegetation drag force may actually extend slightly into the range of small positive y. The boundary layer at the vicinity of the walls is not reproduced by the theory, since we did not make use the condition of vanishing streamwise velocity at the walls, which is difficult to be used in the shallow water formulation.

7.2.2 Maximum friction velocity

The maximum friction velocity defined by the lateral shear stress is determined from the following relation, which is similar to (7.1), and has also been employed by White and Nepf (2007),

$$\tilde{U}_{fM,max}^2 = -\left(\overline{\tilde{U}'\tilde{V}'}\right)_{max}, \tag{7.3}$$

where $\tilde{U}'$ and $\tilde{V}'$ are the fluctuations of $\tilde{U}$ and $\tilde{V}$. The above definition for the friction velocity is employed herein just in the present comparison between theoretical and experimental results. It was not employed when determining the eddy viscosity in (2.11). The predicted $\tilde{U}_{fM,max}$ was found to be located at the interface between the non-vegetated and vegetated zones, while in the experiments of White and Nepf (2007), it was located within $1-2\mathrm{cm}$ of the array edge. This is also because of the slight shift of the observed velocity gradient towards the non-vegetated zone, when comparing to the prediction.

Table 7.4 and Fig 7-10 present a comparison between observed and predicted values of maximum friction velocity $\tilde{U}_{fM,max}$, corresponding to the experimental runs of White and Nepf (2007). The agreement is found to be reasonably good.

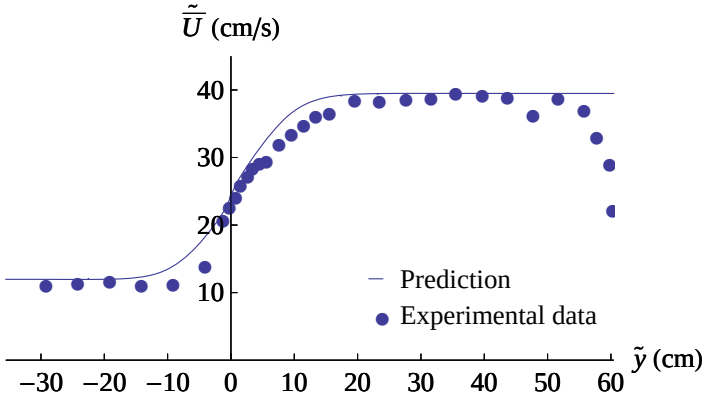

(a)

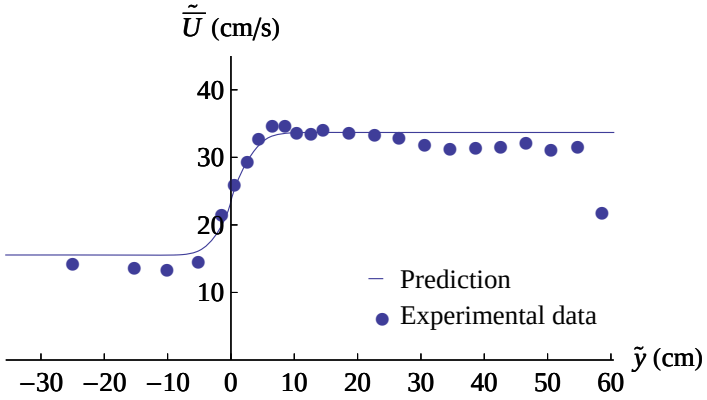

(b)

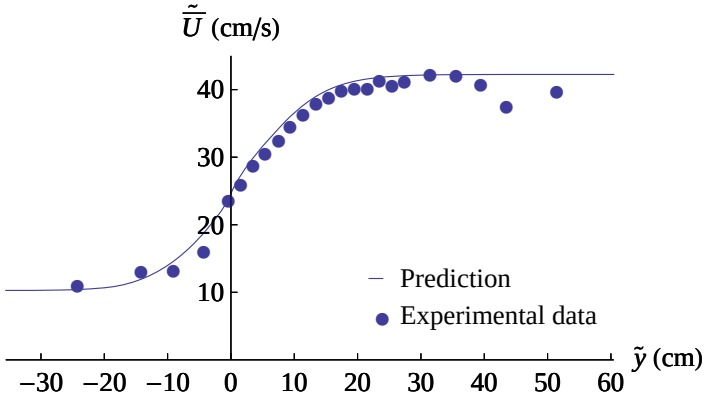

(c)

Figure 7-9: Lateral distribution of time-averaged velocity: (a) run 1; (b) run 2; (c) run 3 (Ikeda et al. (1991)).

Table 7.4: Observed and predicted maximum friction velocity $\tilde{U}_{fM,max}$.

Run, White and Nepf (2007)	I	IV	V	VI	VII	VIII	IX	X
$\tilde{U}_{f,max}$ (cm/s), observed	1.8	2.1	0.4	1.5	1.9	0.4	0.8	3.4
$\tilde{U}_{f,max}$ (cm/s), predicted	1.8	1.8	0.4	1.3	1.9	0.7	1.0	3.2

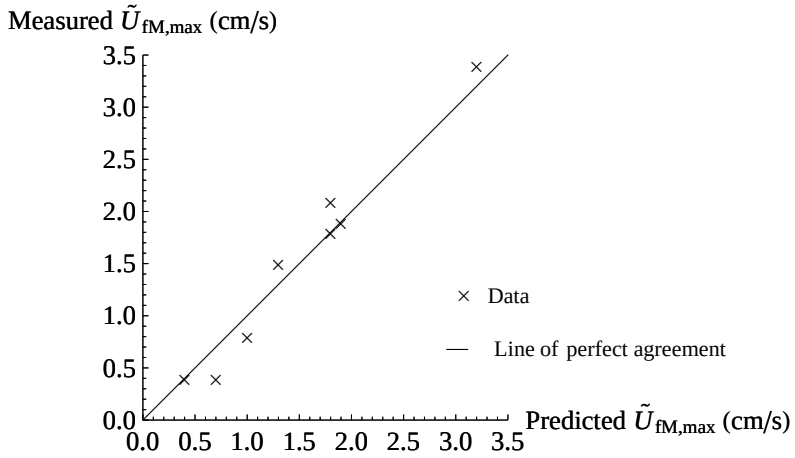

Figure 7-10: Comparison between the predicted and measured maximum friction velocity.

7.2.3 Shear layer width

The shear layer width $\tilde{\Theta}$ is measured by the momentum thickness following White and Nepf (2007),

$$\tilde{\Theta} = \int_{-\tilde{B}_v}^{\tilde{B}} \left[\frac{1}{4} - \left(\frac{\tilde{\overline{U}} - \tilde{U}_A}{\Delta \tilde{U}} \right) \right] d\tilde{y}, \tag{7.4}$$

where $\tilde{U}_A = (\tilde{U}_\infty + \tilde{U}_{-\infty})/2$ and $\Delta \tilde{U} = \tilde{U}_\infty - \tilde{U}_{-\infty}$.

Table 7.5 and Fig. 7-11 present a comparison between observed and predicted values of the shear-layer width at the equilibrium $\tilde{\Theta}$. For most of the runs the agreement may be considered reasonable, with the exception of run VIII.

Table 7.5: Observed and predicted shear layer width at the equilibrium $\tilde{\Theta}$.

Run White and Nepf (2007)	I	IV	V	VI	VII	VIII	IX	X
$\tilde{\Theta}$ (cm), observed	5.1	4.8	4.5	5.4	4.5	4.4	4.4	4.4
$\tilde{\Theta}$ (cm), predicted	4.7	4.5	4.0	4.8	4.7	3.2	4.1	4.9

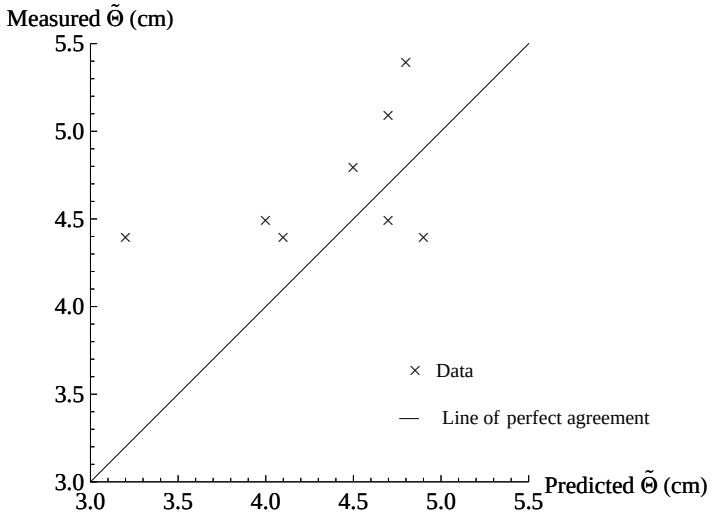

Figure 7-11: Comparison between the predicted and measured shear layer width $\tilde{\Theta}$.

7.2.4 Lateral large-scale kinematic eddy viscosity

Using the velocity fluctuations to express the Reynolds stress, the lateral kinematic eddy viscosity in the equilibrium stage, $\tilde{\nu}_T$, is expressed using Boussinesqs hypothesis as,

$$-\rho\overline{\tilde{U}'\tilde{V}'} = \rho\tilde{\nu}_T\frac{d\overline{\tilde{U}}}{d\tilde{y}}. \tag{7.5}$$

The above expression is a dimensional form of (7.2).

Fig. 7-12 depicts a comparison between the lateral eddy viscosity determined from (7.5) and the lateral eddy viscosity measured by Ikeda et al. (1991). While the value of $\tilde{\nu}_T$ determined by Ikeda et al. (1991) is assumed to be constant along the transverse direction and valid in the regions far from the shear layer, the lateral kinematic eddy viscosity in the perturbed stage obtained herein is only defined at the shear layer and varies along the transverse direction. The values of $\tilde{\nu}_T$ from the present study and from Ikeda et al. (1991) corresponding to runs 2, 3 and 4 showed good agreements. On the other side, the maximum values of $\tilde{\nu}_T$ determined herein from runs 1 and 5 were around 60% of the values from Ikeda et al. (1991).

The sub-depth $\tilde{\nu}_T$ determined from (2.11), and $\tilde{\nu}_T$ determined by Ikeda et al. (1991) (which correspond to the broken lines in Fig. 7-12) are presented in Table 7.6. The sub-

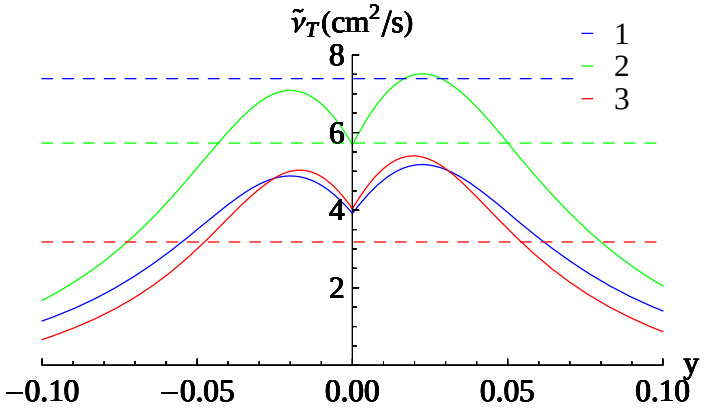

(a)

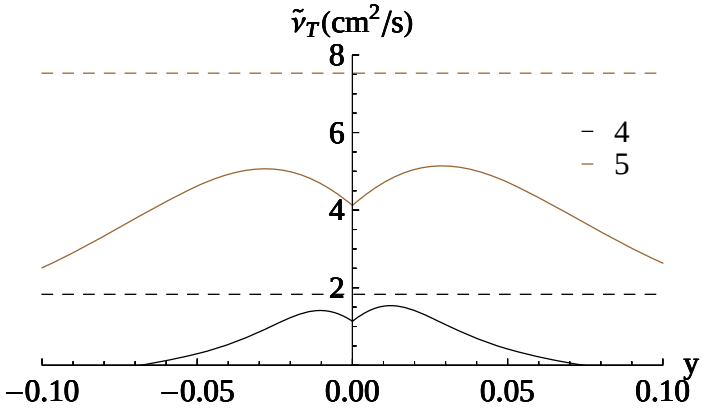

(b)

Figure 7-12: Predicted (continuous lines) and measured (broken lines) lateral kinematic eddy viscosity: (a) runs 1–3; (b) runs 4–5, (Ikeda et al. (1991)).

Table 7.6: Kinematic eddy viscosity employed in the St. Venant shallow water equations.

Run, Ikeda et al. (1991)	1	2	3	4	5
$\tilde{\nu}_T$ (cm^2), present study	1.24	1.84	1.40	0.61	1.82
$\tilde{\nu}_T$ (cm^2), Ikeda et al. (1991)	7.39	5.73	3.18	1.83	7.53

depth eddy viscosity employed herein is significantly smaller because it does not include the effect of the large-scale vortices.

In order to evaluate the growth of the kinematic eddy viscosity from the sub-depth scale to the large scale, we normalize $\tilde{\nu}_T$ using the friction velocity and the flow depth sufficiently far from the vegetated zone, ($\tilde{U}_\infty$ and $\tilde{H}_\infty$, respectively), as follows:

$$\sigma = \frac{\tilde{\nu}_T}{\tilde{U}_{f\infty}\tilde{H}_\infty}. \tag{7.6}$$

Using the above normalization, the value of σ corresponding to the sub-depth eddy viscosity in the present study is $\kappa/6$ ($\cong 0.067$).

Fig. 7-13 shows the kinematic eddy viscosity using the above normalization for runs 1–5 from Ikeda et al. (1991). As expected, all curves surpasses the value of 0.067 around $y = 0$.

The values of σ around $y = 0$ approach the range of 0.15–0.20, which has been employed by Chen and Jirka (1997), Ghidaoui and Kolyshkin (1999) and Prooijen and Uijttewaal (2002). Therefore, the disturbed eddy viscosity determined herein after performing a nonlinear stability analysis approaches the values of eddy viscosity which were initially assumed in the shallow-water formulation of previous studies. This indicates that the development of the linear theory in these studies, including the base state formulation, made use of values of eddy viscosity which may be affected by the large-scale vortices.

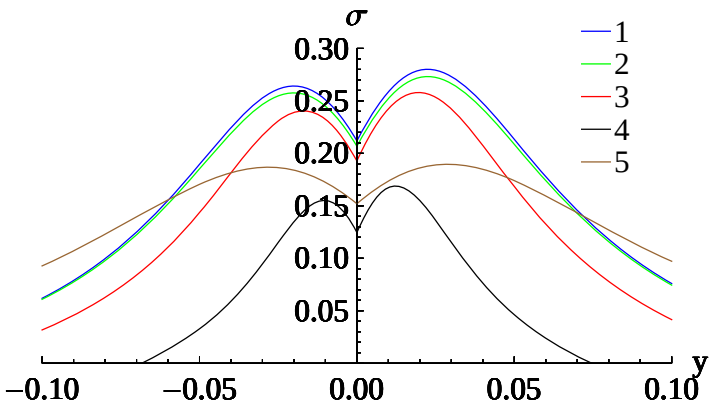

Figure 7-13: Lateral kinematic eddy viscosity σ versus y, at the vicinity of $y = 0$. Runs 1–5 (Ikeda et al. (1991)).

Chapter 8

Conclusions

In this study, we propose new linear and nonlinear stability analyses of flow with a lateral velocity gradient due to the presence of vegetation on one side of an open channel. In the analysis, we employ the St. Venant shallow water equations, and include the Reynolds stresses represented by the kinematic eddy viscosity, which characterizes the sub-depth scale turbulence generated by the bottom friction. In the base state, the velocity distributions inside and outside vegetation are expressed by hyperbolic cotangent and hyperbolic tangent functions squared respectively. These functions are determined analytically, by considering as the base state not the average flow, but the flow without the effects of the large-scale horizontal vortices.

We performed a temporal linear stability analysis by imposing small perturbations on the base state flow velocities and depth. We obtained a set of instability diagrams with respect to six non-dimensional parameters, including a kinematic eddy viscosity parameter, following that we did not employ a formulation for inviscid flow. Our results indicate that, while the base state flow field is unstable in the range of typical, moderate values of the hydraulic parameters, stability is retained in the range of sufficiently small and large vegetation densities, small widths of the vegetated zone, large bed shear effect, large sub-depth eddy viscosity effect, and moderate Froude numbers where the flow is stable to both the transverse mixing and the gravity. The growth rate of perturbations could be evaluated for Froude numbers far from zero because the rigid-lid assumption was not used. The use of a theoretical sub-depth kinematic eddy viscosity unaffected by the lateral motions permitted

a consistent estimation of the growth rate of perturbations. Assuming that the characteristic wavenumber and frequency of perturbations associated with maximum perturbation growth rate correspond to those of vortices realized in experiments, we compare predicted and observed vortex shedding frequencies. The analysis was shown to be capable of predicting the order of magnitude of the vortex shedding frequencies, yet there is a systematic discrepancy in the predicted frequencies when compared to the observed frequencies. This discrepancy, typically in the range of a factor of approximately two, may be caused by the limitation of linear stability analysis.

The nonlinear stability analysis was performed in order to theoretically obtain the fully developed stage of perturbations of a shear flow in a partially vegetated open-channel. The ratio between the undisturbed velocities in the channel was taken as the parameter for expansion in the non-linear analysis, and the corresponding wavenumber for maximum instability was adjusted to this expansion. The theoretical results were validated through a comparison with experimental measurements from previous studies.

The nonlinear model was able to predict the shear layer width and the maximum friction velocity reasonably well. The lateral gradient of the time-averaged velocity was also well represented by the model. The eddy viscosity as a function of the perturbed velocity could be derived and it was found to be coherent with the laterally-disturbed eddy viscosity from previous studies. Therefore, the present model was shown to be capable of predicting the large-scale eddy viscosity from a formulation which included a sub-depth eddy viscosity completely unaffected by the large-scale lateral motions.

Bibliography

Chen, D. and Jirka, G. H. (1997). "Absolute and convective instabilities of plane turbulent wakes in a shallow water layer." *Journal of Fluid Mechanics*, 338, 157–172.

Chu, V. H., Wu, J.-H., and Khayat, R. E. (1991). "Stability of transverse shear flows in shallow open channels." *Journal of Hydraulic Engineering, ASCE*, 117, 1370–1388.

Ghidaoui, M. S. and Kolyshkin, A. A. (1999). "Linear stability analysis of lateral motions in compound open channel." *Journal of Hydraulic Engineering, ASCE*, 125, 871–880.

Ikeda, S., Izumi, N., and Itoh, R. (1991). "Effects of pile dikes on flow retardation and sediment transport." *Journal of Hydraulic Engineering, ASCE*, 117(11), 1459–1478.

Ikeda, S., Ohta, K., and Hasegawa, H. (1994). "Instability-induced horizontal vortices in shallow open-channel flows with an inflection point in skewed velocity profile." *Journal of Hydroscience and Hydraulic Engineering*, 12, 69–84.

Kolyshkin, A. A. and Ghidaoui, M. S. (2002). "Gravitational and shear instabilities in compound and composite channels." *Journal of Hydraulic Engineering, ASCE*, 128, 1076–1086.

Michalke, A. (1964). "On the inviscid instability of hyperbolic tangent velocity profile." *Journal of Fluid Mechanics*, 19, 543–556.

Prooijen, B. C. and Uijttewaal, W. S. J. (2002). "A linear approach for the evolution of coherent structures in shallow mixing layers." *Physics of Fluids*, 14, 4105–4114.

Tamai, N., Asaeda, T., and Ikeda, H. (1986). "Study on generation of periodical large surface eddies in a composite channel flow." *Water Resources Research*, 22(7), 1129–1138.

Tsujimoto, T. (1991). "Open channel flow with bank vegetation." *KHL Communication*, 2, 41–54.

Tsujimoto, T. and Kitamura, T. (1992). "Experimental study on open-channel flow with vegetated zone along side wall." *KHL Progressive Report*, 29–35.

White, B. L. and Nepf, H. M. (2007). "Shear instability and coherent structures in shallow flow adjacent to a porous layer." *Journal of Fluid Mechanics*, 593, 1–32.

Xiaohui, S. and Li, C. W. (2002). "Large eddy simulation of free surface turbulent flow in partially vegetated open channels." *International Journal of Numerical Methods in Fluids*, 39, 919–937.

Appendix A

Notation

The following symbols are used in this paper:

$A =$ amplitude;

$A_e =$ equilibrium amplitude;

$A_R =$ aspect-ratio of the non-vegetated zone;

$a =$ vegetation density parameter;

$B =$ non-vegetated zone width;

$B_v =$ vegetated zone width;

$C_d =$ vegetation drag coefficient;

$C_f =$ bed friction coefficient;

$D_x, D_y =$ streamwise and transverse vegetation drag components, respectively;

$d =$ diameter of cylinders;

$F =$ Froude number;

$G, G_n, J, J_n, K, K_n, L_n, P, P_n =$ linear operators;

$g =$ gravity acceleration;

$H =$ flow depth;

$k =$ wavenumber;

$k_s =$ roughness height;

$l_x, l_y =$ distances between two adjacent cylinders in x and y directions;

$S =$ streamwise bed slope of the channel;

$T =$ period;

$T_{bx}, T_{by} =$ streamwise and transverse bed shear stress components, respectively;

$T_{i,j}\ (i,j = x,y) =$ Reynolds stress tensor;

$T_j(\xi), T_j(\zeta) =$ Chebyshev polynomials in ξ and ζ of degree j;

$t =$ time;

$t_1 =$ time in the slow scale;

$U, V =$ streamwise and transverse velocities, respectively;

$U_0 =$ base state flow velocity;

$U_1, V_1, H_1, U_{11}, V_{11}, H_{11}, U_{00}, U_{20}, V_{20}, H_{20}, U_{22}, V_{22}, H_{22}, U_{31}, V_{31}, H_{31}, U_{33}, V_{33}, H_{33} =$ eigenfunctions;

$U_f =$ friction velocity;

$x, y, z =$ streamwise, transverse and depth coordinates, respectively;

$\alpha =$ vegetation drag parameter;

$\beta =$ bed friction parameter;

$\epsilon =$ sub-depth eddy viscosity parameter;

$\zeta =$ expansion parameter in the multiple scale analysis;

$\eta_0 =$ linear growth rate of the amplitude;

$\eta_1 =$ first Landau constant;

$\Theta =$ shear layer width;

$\kappa =$ Kármán constant;

$\mu =$ equilibrium amplitude phase;

$\nu_T =$ kinematic eddy viscosity;

$\rho =$ water density;

$\sigma =$ kinematic eddy viscosity normalized by the friction velocity and flow depth sufficiently far from the vegetation;

$\phi =$ ratio between the undisturbed velocities in the vegetated zone and the non-vegetated zone;

$\psi =$ base state flow velocity at the interface between the non-vegetated and vegetated zones;

$\Omega =$ growth rate of the perturbations;

$\omega = \omega_r + i\Omega =$ angular frequency.

Subscripts:

$\infty, -\infty =$ far field in the non-vegetated and vegetated zones, respectively;

$c =$ located on the neutral curve;

$M =$ fully developed stage of the perturbations;

$m =$ most unstable mode.

Appendix B

Terms $I_{20}^{(1)}, I_{20}^{(2)}, I_{20}^{(3)}, I_{22}^{(1)}, I_{22}^{(2)}, I_{22}^{(3)}$

$$I_{20}^{(1)} = \begin{cases} \left(2\beta U_{0_c} U_{11} H_{11}^* - V_{11}^* \dfrac{\mathrm{d}U_{11}}{\mathrm{d}y}\right) + \text{c.c.} - \beta\left(2H_{11}H_{11}^* U_{0_c}^2 + 2U_{11}U_{11}^* + V_{11}V_{11}^*\right) & \text{if} \quad 0 \le y \le 1, \\ \dfrac{1}{1+\alpha_c}\left(2\beta U_{0_c} U_{11} H_{11}^* - V_{11}^* \dfrac{\mathrm{d}U_{11}}{\mathrm{d}y}\right) + \text{c.c.} - \beta\left(\dfrac{2H_{11}H_{11}^* U_{0_c}^2}{1+\alpha_c} + 2U_{11}U_{11}^* + V_{11}V_{11}^*\right) & \text{if} \quad -B_v \le y \le 0, \end{cases} \tag{B.1}$$

$$I_{20}^{(2)} = \begin{cases} \left(\beta U_{0_c} V_{11} H_{11}^* - V_{11} \dfrac{\mathrm{d}V_{11}^*}{\mathrm{d}y} - \beta U_{11} V_{11}^*\right) + \text{c.c} + \mathrm{i}k_c U_{11} V_{11}^* - \text{c.c.} & \text{if} \quad 0 \le y \le 1, \\ \left[\dfrac{1}{1+\alpha_c}\left(\beta U_{0_c} V_{11} H_{11}^* - V_{11} \dfrac{\mathrm{d}V_{11}^*}{\mathrm{d}y}\right) - \beta U_{11} V_{11}^*\right] + \text{c.c} + \dfrac{\mathrm{i}k_c U_{11} V_{11}^*}{1+\alpha_c} - \text{c.c.} & \text{if} \quad -B_v \le y \le 0, \end{cases} \tag{B.2}$$

$$I_{20}^{(3)} = -\left[\left(V_{11}\frac{\mathrm{d}H_{11}^{*}}{\mathrm{d}y} + H_{11}\frac{\mathrm{d}V_{11}^{*}}{\mathrm{d}y}\right) + \text{c.c.}\right] \tag{B.3}$$

$$I_{22}^{(1)} = \begin{cases} 2\beta U_{0_c}U_{11}H_{11} - V_{11}\dfrac{\mathrm{d}U_{11}}{\mathrm{d}y} - \beta U_{0_c}^2 H_{11}^2 - \mathrm{i}k_c U_{11}^2 - \beta U_{11}^2 - \dfrac{\beta}{2}V_{11}^2 & \text{if} \quad 0 \le y \le 1, \\ \dfrac{1}{1+\alpha_c}\left(2\beta U_{0_c}U_{11}H_{11} - V_{11}\dfrac{\mathrm{d}U_{11}}{\mathrm{d}y} - \beta U_{0_c}^2 H_{11}^2 - \mathrm{i}k_c U_{11}^2\right) - \beta U_{11}^2 - \dfrac{\beta}{2}V_{11}^2 & \text{if} \quad -B_v \le y \le 0, \end{cases} \tag{B.4}$$

$$I_{22}^{(2)} = \begin{cases} \beta U_{0_c}V_{11}H_{11} - V_{11}\dfrac{\mathrm{d}V_{11}}{\mathrm{d}y} - \mathrm{i}k_c U_{11}V_{11} - \beta U_{11}V_{11} & \text{if} \quad 0 \le y \le 1, \\ \dfrac{1}{1+\alpha_c}\left(\beta U_{0_c}V_{11}H_{11} - V_{11}\dfrac{\mathrm{d}V_{11}}{\mathrm{d}y} - \mathrm{i}k_c U_{11}V_{11}\right) - \beta U_{11}V_{11} & \text{if} \quad -B_v \le y \le 0, \end{cases} \tag{B.5}$$

$$I_{22}^{(3)} = -2\mathrm{i}k_c U_{11}H_{11} - V_{11}\frac{\mathrm{d}H_{11}}{\mathrm{d}y} - H_{11}\frac{\mathrm{d}V_{11}}{\mathrm{d}y} \tag{B.6}$$